Contents lists available at ScienceDirect

Remote Sensing of Environment

The EnMAP imaging spectroscopy mission towards operations

Tobias Storch [a,*], Hans-Peter Honold [e], Sabine Chabrillat [g,h], Martin Habermeyer [a], Paul Tucker [e], Maximilian Brell [g], Andreas Ohndorf [d], Katrin Wirth [d], Matthias Betz [e], Michael Kuchler [e], Helmut Mühle [a], Emiliano Carmona [a], Simon Baur [e], Martin Mücke [e], Sebastian Löw [d], Daniel Schulze [d], Steffen Zimmermann [d], Christoph Lenzen [d], Sebastian Wiesner [d], Saika Aida [d], Ralph Kahle [d], Peter Willburger [d], Sebastian Hartung [b], Daniele Dietrich [a], Nicolae Plesia [a], Mirco Tegler [b], Katharina Schork [a], Kevin Alonso [a], David Marshall [a], Birgit Gerasch [c], Peter Schwind [a], Miguel Pato [a], Mathias Schneider [a], Raquel de los Reyes [a], Maximilian Langheinrich [a], Julian Wenzel [f], Martin Bachmann [a], Stefanie Holzwarth [a], Nicole Pinnel [a], Luis Guanter [i], Karl Segl [g], Daniel Scheffler [g], Saskia Foerster [g], Niklas Bohn [g,l], Astrid Bracher [j], Mariana A. Soppa [j], Ferran Gascon [k], Rob Green [l], Raymond Kokaly [m], Jose Moreno [n], Cindy Ong [o], Manuela Sornig [p], Ricarda Wernitz [p], Klaus Bagschik [p], Detlef Reintsema [p], Laura La Porta [p], Anke Schickling [p], Sebastian Fischer [p]

[a] German Aerospace Center (DLR), Earth Observation Center (EOC), Weßling, Germany
[b] German Aerospace Center (DLR), Earth Observation Center (EOC), Neustrelitz, Germany
[c] German Aerospace Center (DLR), Earth Observation Center (EOC), Berlin, Germany
[d] German Aerospace Center (DLR), German Space Operations Center (GSOC), Weßling, Germany
[e] OHB System AG, Weßling, Germany
[f] EOMAP GmbH & Co. KG, Seefeld, Germany
[g] GFZ German Research Centre for Geosciences, Potsdam, Germany
[h] Leibniz University Hannover, Institute of Soil Science, Hannover, Germany
[i] Universitat Politecnica de Valencia, Research Institute of Water and Environmental Engineering (IIAMA), Valencia, Spain
[j] Alfred Wegener Institute (AWI), Helmholtz Centre for Polar and Marine Research, Bremerhaven, Germany
[k] European Space Agency (ESA), Frascati, Italy
[l] National Aeronautic and Space Agency (NASA), Jet Propulsion Laboratory (JPL), Pasadena, CA, USA
[m] U.S. Geological Survey (USGS), Geology, Geophysics, and Geochemistry Science Center, Lakewood, CO, USA
[n] Universitat de Valencia, Faculty of Physics, Department of Earth Physics and Thermodynamics, Valencia, Spain
[o] Commonwealth Scientific and Industrial Research Organisation (CSIRO), Bentley WA, Australia
[p] German Aerospace Center (DLR), Space Agency, Bonn, Germany

ARTICLE INFO

ABSTRACT

EnMAP (Environmental Mapping and Analysis Program) is a high-resolution imaging spectroscopy remote sensing mission that was successfully launched on April 1st, 2022. Equipped with a prism-based dual-spectrometer, EnMAP performs observations in the spectral range between 418.2 nm and 2445.5 nm with 224 bands and a high radiometric and spectral accuracy and stability. EnMAP products, with a ground instantaneous field-of-view of 30 m×30 m at a swath width of 30 km, allow for the qualitative and quantitative analysis of surface variables from frequently and consistently acquired observations on a global scale. This article presents the EnMAP mission and details the activities and results of the Launch and Early Orbit and Commissioning Phases until November 1st, 2022. The mission capabilities and expected performances for the operational Routine Phase are provided for existing and future EnMAP users.

1. Introduction

EnMAP (Environmental Mapping and Analysis Program, EnMAP.org, 2022) is a high-resolution imaging spectroscopy remote sensing mission. Its main objective is to measure, derive and analyze qualitative and quantitative diagnostic surface variables describing key processes on the Earth (Guanter et al., 2015) which are frequently and consistently acquirable on a global scale. Therefore, based on specific user requests, the mission provides high-fidelity samples for a swath width of 30 km, a swath length of up to 5550 km per day with 30 m × 30 m pixels and 224 bands between 418.2 nm and 2445.5 nm acquired by a prism-based push-broom dual-spectrometer. The satellite tilting capabilities of ±30 deg in a Sun-synchronous repeat orbit of 27 days reduces the target revisit frequency to less than 4 days.

The satellite was successfully launched on April 1st, 2022, with an expected operational lifetime of more than five years. EnMAP will significantly contribute to the availability of space-based imaging spectroscopy products to provide information about the status of different ecosystems—mainly focusing on issues related to soil, geology, agriculture, forestry, urban areas, aquatic systems, ecosystem transitions, associated sciences and applications. This article details the activities performed since launch and illustrates the status at the first day of the operational Routine Phase, namely on November 2nd, 2022, after successful completion of the Launch and Early Orbit Phase (LEOP) and Commissioning Phase (CP) as well as a major review conducted between October 7th and 28th, 2022.

The next sections detail: the missions related to EnMAP; the EnMAP mission architecture from an overview of the three segments and the major mission parameters; the EnMAP mission status and operations during the major mission activities of LEOP and CP; the user interfaces; and the performed observations. Section 2 analyzes the spectral, radiometric and geometric calibrations and Section 3 characterizes the processors which incorporate the calibrations and provide the user products at three processing levels. The results of the data quality assessment and independent product validation are analyzed here. Finally, Section 4 provides the conclusions. (See Supplements.0 for a list of all abbreviations.)

1.1. Related missions

Most activities in imaging spectroscopy in the last decades have been based on airborne imaging spectrometers covering the visible and near-infrared (VNIR, roughly 400 nm to 1000 nm) and shortwave-infrared (SWIR, roughly 1000 nm to 2500 nm) reflective spectral ranges. Notably, the Airborne Visible/Infrared Imaging Spectrometer (AVIRIS), realized and operated by the NASA Jet Propulsion Laboratory, CA, USA, has been used in a large number of imaging spectroscopy campaigns for the last decades (Green et al., 1998). In 2011 DLR (German Aerospace Center) procured an airborne HySpex system to act as the so-called EnMAP simulator to prepare for the mission (Köhler, 2016). Despite the large potential of imaging spectroscopy, only relatively few spaceborne imaging spectrometers have been launched. In particular, the technology demonstration mission Hyperion on Earth Observing-1 (EO-1), realized and operated by NASA (National Aeronautics and Space Administration) and USGS (U.S. Geological Survey), has been the main provider of satellite hyperspectral data for the last few years (2000-2017, Pearlman et al., 2003). Recently DESIS (DLR Earth Sensing Imaging Spectrometer, in 2018, Alonso et al., 2019), PRISMA (PRecursore IperSpettrale della Missione Applicativa, in 2019, Cogliati et al., 2021), HISUI (Hyperspectral Imager SUIte, in 2019, Urai et al., 2021), and EMIT (Earth surface Mineral dust source InvesTigation, in 2022, Connelly et al., 2021) were launched. Existing and future imaging spectroscopy missions will focus on the atmosphere or oceans at coarser spatial resolutions specifically covering the VNIR (Barnes et al., 2003; Werdell et al., 2019) or on specific aspects such as fluorescence (Drusch et al., 2017). Furthermore, future imaging spectroscopy mapping

Table 1
Achieved vs. required values for major mission parameters.

Mission parameter	Achieved	Required	Fulfilled
Spectral range (nm)	418.2–2445.5	420.0–2450.0	Yes[a]
Spectral sampling distance VNIR/SWIR (nm)	6.4/10.0	6.5/10.0	Yes
Spectral accuracy (nm)	≤0.5	0.5	Yes
Radiometric accuracy (%)	≤5.0	5.0	Yes[b]
Radiometric stability[c] (%)	≤2.5	2.5	Yes
SNR for VNIR/SWIR[d]	620:1/230:1	500:1/150:1	Yes
Geolocation accuracy without/with GCPs[e] (m)	55/20	100/30	Yes
Co-registration VNIR-to-SWIR (pixel)	0.4	0.3	No[f]
Ground instantaneous field-of-view (m × m)	30×30	30×30	Yes
Swath width/length/day (km)	30/5550	30/5000	Yes
Product levels for users	1B, 1C, 2A	1B, 1C, 2A	Yes

[a] SWIR band at 2445.5 nm with 7.2 nm width covers spectral range up to 2450 nm; spectral overlap between VNIR and SWIR from 902.2 nm to 993.0 nm.
[b] More statistics for more precise evaluation of absolute accuracy are expected in 2023; algorithms for minimizing striping effects (≤0.4%) are planned for the middle of 2023.
[c] Relative difference between consecutive calibrations.
[d] SNR (Signal-to-Noise Ratio) for VNIR at 495 nm/SWIR at 2200 nm.
[e] Availability of automatically extracted GCPs (Ground Control Points) depends on image content.
[f] Improvements based on further geometric calibrations are planned for the middle of 2023.

systems include demonstration missions (Carbon Mapper; Keremedjiev et al., 2022) and operational missions planned for after 2027 such as the CHIME (Copernicus Hyperspectral Imaging Mission for the Environment, Celesti et al., 2022) and SBG (Surface Biology and Geology, Thompson et al., 2022).

1.2. Mission architecture and overview

The EnMAP mission is organized in three main entities:

- The EnMAP Space Segment is owned by the DLR Space Agency, who contracted OHB System AG for the construction of the satellite (Sang et al., 2008), and is also responsible for the Mission Management.
- The EnMAP Ground Segment is realized and operated by the DLR institutes DFD (German Remote Sensing Data Center), MF (Remote Sensing Technology Institute) and RB (German Space Operations Center) (Storch et al., 2013).
- The EnMAP Science and User Segment is represented by the GFZ German Research Centre for Geosciences (EnMAP.org, 2022, for the science plan).

The mission parameters are based on the scientific objectives of the mission and formulated as requirements applicable to the space and ground segments during all pre- and post-launch phases. The major mission parameters are listed in Table 1, stating their required and achieved values at the end of the CP. Further improvements on aspects such as radiometric and geometric accuracy are planned for the middle of 2023.

1.2.1. Space segment

The EnMAP Space Segment with a satellite mass of 916 kg and dimensions of 3.1 m × 2.0 m × 1.7 m is composed of: the platform providing power and thermal stability, orbit and attitude control; satellite management and control; S-band downlink/uplink for telemetry/telecommand (TM/TC) data transmission/reception and of the

payload providing X-band downlink for payload data transmission; payload data storage; and finally the instrument itself.

The main instrument of EnMAP is the Hyper-Spectral Imager (HSI, Kaufmann et al., 2016). The HSI has several mission requirements with the goal to deliver high spectral, radiometric and geometric accuracy at high instrument stability. The HSI is a push-broom sensor with a prism-based dual-spectrometer. Each sensor, namely the VNIR and SWIR operate independently and has a slightly separated Lines-Of-Sight, requiring the combination of both data streams during on-ground processing.

Both sensors feature two gain settings each, namely low gain and high gain. The VNIR instrument is operated in automatic gain mode, where each pixel can switch to low gain setting if the signal is large enough. For SWIR a fixed gain setting is used, where bands below 1980 nm are in low gain and bands above 1980 nm in high gain. The different gain settings for VNIR and SWIR are due to fundamental differences in the detector technology and architecture.

The VNIR spectrometer covers the spectral range from 418.2 nm to 993.0 nm with a spectral sampling distance between 4.7 nm and 8.2 nm (6.4 nm on average) over 91 bands. The SWIR spectrometer covers the spectral range from 902.2 nm to 2445.5 nm with a spectral sampling distance between 7.5 nm and 12.0 nm (10.0 nm on average) over 155 bands, where only 133 bands are transmitted in order to avoid the ranges with strong atmospheric absorption. The spectral range of both sensors overlap in the range from 902.2 nm to 993.0 nm. The SWIR detector assembly including the front-end electronics is fully redundant which allows to switch from the nominal SWIR-A detector to the redundant SWIR-B detector in case of a severe malfunction.

The spectral and radiometric stability between two consecutive calibration measurements is better than 0.5 nm and well within the 2.5% at-sensor radiance level which is confirmed in-flight using the satellite calibration equipment as well as Earth Observation (EO) acquisitions. The Signal-to-Noise Ratio (SNR) for the reference radiance level (which is defined by 30% surface albedo, 30 deg Sun zenith angle, ground at sea level, and 40 km visibility with rural atmosphere) is 620:1 at 495 nm and 230:1 at 2200 nm on the first day of the operational Routine Phase, where the radiometric resolution is 14 bits. Although radiometric requirements are fulfilled, in particular on the relative and absolute radiometric accuracy of 2.5% and 5.0%, striping effects are sometimes visible in the images and will be significantly reduced for all data by the incorporation of an algorithm in the on-ground processing chain planned for the middle of 2023.

Each detector array has 1000 valid pixels in spatial direction with an Instantaneous Field-Of-View (IFOV) of 9.5 arcsec (45 μrad). The Sun-synchronous orbit of EnMAP has a mean Local Time at Descending Node (LTDN) of 11:00 h at 642 km mean altitude (and 97.978 deg inclination) resulting in a ground IFOV of 30 m × 30 m and a swath width (across-track) of 30 km. These orbital parameters allow observations at any location on the globe with comparable illumination conditions and a maximum reflected solar input radiance at the sensor with an acceptable risk for cloud coverage. The ground-track reference orbit comprises 398 orbits within a repeat cycle of 27 days (Kahle et al., 2019). The pointing capabilities of the satellite, namely by ±30 deg across-track, allow for acquisitions of the same target every 4 days. Each EO acquisition is planned based on a specific user request defining information such as acceptable cloud coverage, acceptable tilt angle, center coordinate, time-frame and swath length (along-track). The maximum swath length of each EO acquisition is limited to approx. 990 km, the minimum gap between acquisitions is approx. 3000 km and the maximum acquisition capacity per day is 5550 km.

1.2.2. Ground segment

The EnMAP Ground Segment is the interface between the Space Segment and the Science and User Segment. It comprises functionalities to perform the planning of imaging, communication and orbit maneuver operations, provision of orbit and attitude data, command and control

of the satellite, ground station networks for S- and X-band, reception of satellite data, long-term archiving, search and view services as well as delivery of products. Furthermore, a fully-automatic processing chain is operated for the radiometric correction, orthorectification, atmospheric compensation, instrument calibration operations and the quality control of the products. These image products at three processing levels are free and openly available to the user community (see EnMAP.org, 2022, for details on the license):

- Level 1B (L1B) products are raw instrument data corrected to Top-Of-Atmosphere (TOA) radiance in sensor geometry.
- Level 1C (L1C) products are L1B products orthorectified to a user selected map projection and resampling model.
- Level 2A (L2A) products are L1C products compensated for atmospheric effects to Bottom-Of-Atmosphere (BOA) reflectance with separate algorithms for land and water applications.

The EnMAP mission interfaces to international users through the EnMAP portal at EnMAP.org (2022) with official information related to EnMAP and links for ordering acquisitions and products. Additionally, it is planned to release L2A snapshots of the archived image products through other distributors in the future.

1.2.3. Science and user segment

The EnMAP Science Segment addresses aspects such as Cal/Val activities for the improvement of the sensor performance and product quality as well as scientific and application research to fully exploit the potential of EnMAP. The EnMAP User Segment is the community of German and international users ordering acquisitions and accessing the EnMAP products.

1.3. Mission status and operations

The mission was successfully launched on a Falcon 9 rocket by SpaceX on April 1st, 2022, at 16:24 UTC in Florida, USA. Separation occurred at 16:37 UTC.

After launch, during LEOP and CP, the platform and payload were successfully operated for seven months forming a solid basis for routine operations. During these phases, a number of issues were identified, investigated and resolved. For each of the encountered issues, mitigation measures were developed which either have been realized or are planned during the first months of routine operations and have needed or will need modifications on both sides, space and ground segment.

Since November 2nd, 2022, EnMAP is in its Routine Phase and operations are expected to last until at least April 14th, 2027, with plenty of propellant margin.

1.3.1. Launch and early orbit phase

The LEOP was performed until April 14th, 2022. The first activity of operations was to establish the bi-directional communication connection, namely telemetry/telecommand (TM/TC), between the satellite and the S-band ground station network. The work and behavior of the S-band ground station network was nominal with a reliability of 99.3%. After LEOP it was sufficient to schedule Weilheim, Germany, as the baseline (Gnat, 2022, see Supplements.3 for details).

Afterwards, initial configurations were successfully performed whereby all launch locks were released and the Attitude Control System (ACS) and Orbit Control System (OCS) were checked out such that the target orbit was reached on April 9th, 2022. Since then through orbit maintenance maneuvers the satellite orbit is controlled with respect to the Earth-fixed reference track over the entire orbit, analogous to a rim, with a control box defined by lateral deviation of at most 22 km and altitude deviation of at most 6 km (Kahle et al., 2022, see Supplements.2 for details).

Further, the payload data storage, the simplex payload data transmission from the satellite to the X-band ground station network, the instrument control and processing unit of the instrument were checked

out. The first X-band data reception was successfully completed on April 8th, 2022, for so-called auxiliary data which are recorded in the payload data storage and on April 27th, 2022, for instrument data. Since then a reliability of 99.6% was achieved for the X-band ground station Neustrelitz, Germany, (Damerow et al., 2010, see Supplements.4 for details). By the beginning of 2023 the integration of the additional X-band ground station Inuvik, Canada, is expected which will further increase the number of EO acquisitions in general and in particular over Europe, because of the good performance of the satellite power system.

Having stable platform and payload environments well within the limits enabled an early startup of the active instrument thermal control. This comprises several mini Loop Heat Pipes (LHP) for each detector assembly. Issues with one LHP for a compressor were encountered which did not prevent instrument operations (see Supplements.1 for details). In particular, the cooling performance of the compressor itself and the optical performance of the instrument are unaffected and the issue has been mitigated by accounting for the maximum operational duration of the instrument in a given time-span. Finally, some hot and cold redundant systems as well as non-nominal modes were successfully checked out.

1.3.2. Commissioning phase

After successfully finishing the tasks of the LEOP, the CP ran until November 1st, 2022, with the first image acquisition on April 27th, 2022, at 09:29 UTC over Istanbul, Turkey (westward tilt of 4.6 deg and approx. 180 km swath length; pre-flight calibration tables were considered; see Fig. 1 for an excerpt of approx. 54 km swath length), after the mechanisms were calibrated and the instrument with the VNIR camera and SWIR-A camera as well as the payload data transmission were completely checked out. These first instrument observations gave a good indication of the high-quality data to be expected from EnMAP—even prior to further improved performance using in-flight calibration means. The instrument data were screened for possible ground-to-orbit effects such as gravity release, air-to-vacuum effects and slippage of interfaces. All effects were within expectations leading to the conclusion that pre-flight performances had successfully been transferred to in-flight.

The platform and payload are operable and provide EO acquisitions and calibration measurements as requested. All elements of the satellite, namely the power, thermal, attitude and orbit control as well as data handling, are working well within required performance and allow the satellite to be operated within the multi-mission control centers. In total 80 sensor parameters of the instrument, namely 68 temperature sensors and 12 electrical sensors, are regularly checked. The instrument performs well and almost all parameters are in the nominal range.

An initial degradation of the response of the VNIR detector was identified at the beginning of the CP. During the CP, a gradual slow-down of degradation was observed as detailed in Section 2.3.1. Whilst attempts to influence the degradation rate by restarting some systems were not successful, the observed slow down of the degradation has rendered any further attempts unnecessary. Despite the degradation, it is expected that the requirements, in particular on the radiometric accuracy and Signal-to-Noise Ratio (SNR), will continue to be met over the mission lifetime. For best possible radiometric performance, dynamic radiometric calibration coefficients will be incorporated in the calibration and processor by the middle of 2023 for all data in the period where degradation occurred.

1.4. User interfaces

Users have to register through the EnMAP Portal at EnMAP.org (2022) to order acquisitions (as Cat-1 for scientific users and Cat-2 for commercial users) or products (as Catalogue user or Cat-1, Cat-2) (Habermeyer et al., 2019; EnMAP.org, 2022, for the detailed user manual). Registration for different roles is possible. Improvements on the usability of the various aspects of the EnMAP Portal are continuously performed.

1.4.1. Order products

To make handling of the EnMAP products more convenient for users, EO acquisitions of swath length $n \times 30$ km are split into n tiles of swath length 30 km and are then long-term archived. All users can search for and filter the archived products in a freely available open product catalogue. For each tile, users can inspect the product parameters and quicklooks. All registered users are able to order tiles with user-specified processing options for free. Because of the various processing levels and options and to always consider the most up-to-date processor version, each product is specifically generated for each order. Furthermore, the quicklooks of tiles are also available with mapping, coverage and feature services. Users can visualize quicklooks on a map and download coverages of quicklooks.

Orders are handled completely automatically. This includes the submission of the orders to the operational processing system which processes the tiles according to the processing options. Once processing is finished, the products are put on the delivery SFTP (Secure File Transfer Protocol) server and the user is notified via email that the products are downloadable.

1.4.2. Order acquisitions

If a user is registered as Cat-1 at the portal to order acquisitions, the user submits a proposal with information such as the required number of EO acquisitions, whether related campaigns are planned, and responds to one of the two Announcement-of-Opportunities (AOs). AO#1 is the general AO and AO#2 is the special AO dedicated to Long-Term Ecosystem Monitoring. When the proposal is accepted after a scientific review, requests are orderable by the user based on a robust menu- and map-based web application using a custom GIS (Geographic Information System). Calibration measurements are only orderable by users responsible for operations. The portal to order products is also accessible through the portal to order acquisitions for an improved user experience. Final adjustments and improvements to the proposal handling and ordering of EO acquisitions will be incorporated in the first two months of routine operations.

Ordered acquisitions are considered in the timeline of satellite activities. In case of conflicts, ordered acquisitions are prioritized not only according to static information like the underlying priority of the request (from highest to lowest: users responsible for operations, users related to the International Charter Space and Major Disasters, Cat-1 (related campaigns: yes), Cat-1 (related campaigns: no), Cat-2, others), but also based on historical and predicted cloud coverage information taking satellite constraints such as data storage and power availability into account. By the middle of 2023 the minimum duration between two consecutive EO acquisitions is expected to decrease from 390 s, approx. 3000 km, to 125 s, approx. 900 km. All information is immediately incorporated into the timeline and users are notified when the status of their request changes.

Although the pointing knowledge is within the requirements, namely a geometric accuracy of approx. 55 m is achieved and improved by on-ground processing to approx. 20 m with respect to a used reference image, the pointing accuracy is expected to improve in the first two months of routine operations. Occasionally a non-constant along-track shift of up to 12 km is observed between the planned area (requested observation) and the acquired area (delivered product) for tilt angles that are well off nadir. To guarantee a complete coverage of the area-of-interest, it is suggested to users to extend the swath length by 30 km until the improvement is operational.

1.5. Observations

When the instrument data, calibration tables and auxiliary products for orbit and attitude are available, the data streams are automatically processed to Level 0 (L0) products. Based on the acquisition or based on an order from the catalogue, the L0 product is automatically processed to an L1B, L1C or L2A product according to the user-specified processing options.
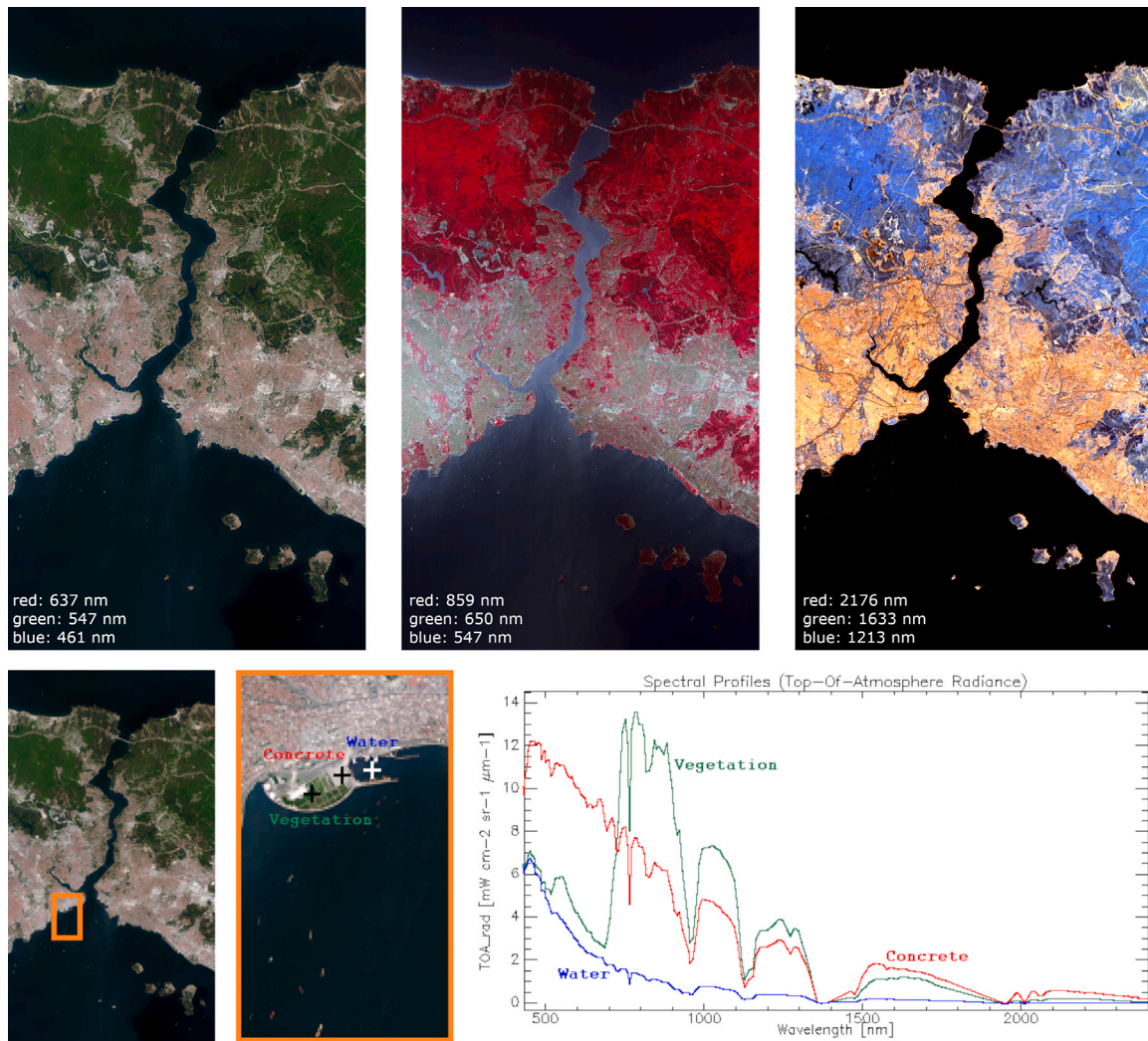
Fig. 1. First image, 27.04.2022, 09:29 UTC, Istanbul, Turkey; Top: Three band combinations; Bottom: Three selected spectra from the marked areas; EnMAP data © DLR 2022. All rights reserved.

Table 2
Number and size (in GByte) of archived EO tiles, EO acquisitions (acq.) and calibration measurements (Cal.).

Month	EO tiles	EO acq.	EO acq.	Cal.	Cal.	EO	Cal.
Archived:	*Yes*	*Yes*	*No*	*Yes*	*No*	**Size**	**Size**
04 (≤14)	0	0	0	0	0	0.0	0.0
04 (>14)	6	2	0	2	0	5.0	1.7
05	108	11	0	0	0	54.6	28.9
06	1,630	303	0	13	0	818.3	79.6
07	2,555	506	12	10	0	1282.3	54.0
08	2,884	569	0	10	0	1447.5	42.8
09	3,303	522	97	9	1	1648.6	32.3
10	2,925	508	4	12	0	1468.1	46.4
11 (≤1)	87	8	0	0	0	43.6	0.0
Total	**13,498**	**2429**	**113**	**62**	**1**	**6768.1**	**285.7**

Approximately 13,500 tiles were successfully archived during the CP which corresponds to an area larger than Europe. Fig. 2 illustrates the geographical location (see Supplements.5 for details). A reliability of 95.0%, the percentage of successfully archived acquisitions to all acquisitions, was achieved, as illustrated in Table 2.

A re-processing of the entire archive is planned during 2023 to further improve the consistency and quality of the archived metadata (e.g.

the cloud coverage, the separation in high and low quality), quicklooks (to consider adjusted thresholds of quality control based on in-flight performance), geometric accuracy and especially the spatial VNIR-to-SWIR co-registration. However, for the generation of the user products, the most up-to-date processor version and spectral and radiometric calibration tables are always used.

2. Spectral, radiometric and geometric calibrations

2.1. Overview

The satellite is equipped with several elements which enable periodic in-flight calibrations and monitoring (Baur et al., 2019). Based on the in-flight measurements, updates can be made to: the radiometric coefficients, namely radiometric calibration, Response Non-Uniformity (RNU) and gain matching; the central wavelengths and thus the Spectral Response Functions (SRFs); the dead pixels mask; the deep space reference; the dark signal reference; and the linearity behavior. The first integrating sphere (on the satellite) is coated with a doped diffusor material and is used for spectral calibration. The second integrating sphere (on the satellite) is coated with a white Spectralon® for relative radiometric stability monitoring. Both are illuminated with a 10 W Tungsten halogen lamp and a white LED (Light Emitting Diode). These calibration measurements also allow for the regular update of the dead
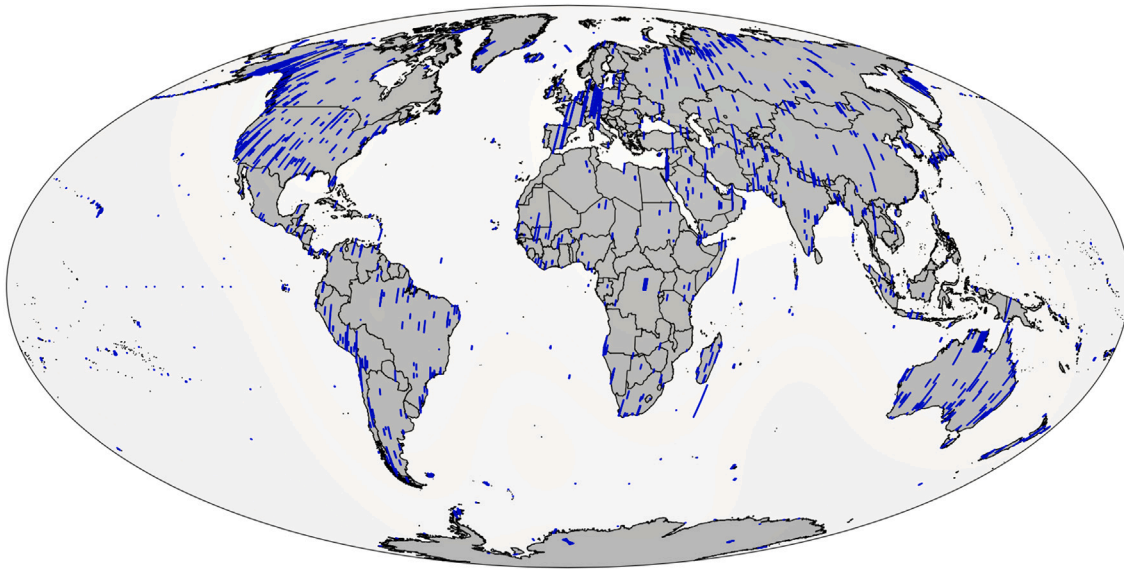
Fig. 2. Geographical location of archived EO tiles (blue).

pixel mask containing, for example, hot, cold, stuck and flickering pixels. Approximately 0.15% of VNIR pixels and 1.15% of SWIR pixels are contained in the mask and no clusters are identified. Absolute radiometric calibration is based on Sun calibration measurements with a full-aperture diffusor switching the diffusor protective hatch and the Sun diffusor hatch. Linearity LEDs are located in front of the detectors to monitor the linearity by measuring the signal at constant illumination and increasing integration times. The final calibration element is the shutter calibration mechanism which enables closed shutter measurements, namely with no light, to be acquired before and after EO acquisitions and calibration measurements for dark signal subtraction. Additional measurements looking into deep space are performed to monitor the thermal emission from the shutter.

2.2. Spectral calibration

Spectral characterization is performed based on measurements of the doped integrating sphere which induces spectral features for the assessment of changes in the center wavelengths and thus updates to the spectral calibration table, if necessary (Storch et al., 2018b). The in-flight measurements are compared to a reference measurement via a merit function with four independent parameters: two for radiometry and two for spectral optimization. The function is minimized during the optimization procedure, which makes iterative shifts to the reference spectrum, the amplitude and the offset until the assessment criteria is fulfilled.

Spectral calibration measurements are made on a bi-weekly basis and 12 were acquired during CP. After launch average shifts in the central wavelengths of approx. 3 nm in VNIR and SWIR were observed as illustrated in Fig. 3, which was expected due to air–vacuum transition and gravity release, and resulted in updates to the spectral calibration table. As of June 25th, 2022, a good spectral stability has been achieved. Fluctuations in the change in center wavelengths between consecutive calibration measurements are within the constraints of the optimization method, namely less than 0.09 nm corresponding to 0.033% in VNIR and less than 0.01 nm corresponding to 0.004% in SWIR. The VNIR and SWIR Center Wavelength (CW) from the latest calibration table on June 25th, 2022, are shown in Fig. 4 along with the Full Width at Half Maximum (FWHM), which was measured pre-flight and is not updated in-flight.

Furthermore, regular and systematic monitoring of the functional units of the instrument are performed concerning stability and trends.

First, special attention is paid to temperature stability as this can affect the dark signal, for example. All temperatures are stable within specified temperature ranges with the exception of the compressor as mentioned in Section 1.3.1. Second, special attend is paid to long-term behavior of calibrations, for which all generated calibration and reference tables are used. These statistics and results are consistent with those of the calibration activities (see Supplements.6 for details).

2.3. Radiometric calibration

Some effects are not measurable during operations, like spectral and spatial straylight; the pre-flight radiometric calibration (Baur et al., 2022) provided the first reference measurements of the satellite calibration equipment.

2.3.1. Relative radiometric

The stability of the instrument is assessed by observing the light from the white integrating sphere which provides five levels of radiance intensity (Storch et al., 2020).

These measurements are made on a weekly basis and 19 were acquired during CP. Through these calibrations, it became clear that the VNIR sensor was experiencing an unexpected and rapid degradation in performance, as illustrated in Fig. 5. Note that these are characterization measurements to illustrate the effect which is largely removed by the calibration. Over six months of observations, the sensor degraded by about 7.5% on average between the first in-flight measurement on May 3rd, 2022, and the last in-flight measurement during the CP on October 26th, 2022. The exact root cause cannot be ascertained, but detailed investigation of the effects makes contamination unlikely. Furthermore, degradation is not homogeneous across the focal plane: the highest degradation occurs in the first spectral pixels (>8% on average) and in the central spatial pixels (>9% on average). Comparing the first and last in-flight measurements, several features are apparent in the degradation pattern. A similar degradation behavior was confirmed through other calibration measurements, namely linearity, spectral and absolute radiometric calibration measurements.

Based on consecutive calibration measurements, the magnitude of the degradation appears to be dropping: on June 20th, 2022, the average decay per day was found to be 0.063%, but by October 26th, 2022, the degradation had decreased to 0.021%. The individual degradation values fluctuate significantly over time and for the different calibration types because they are obtained from measurements that
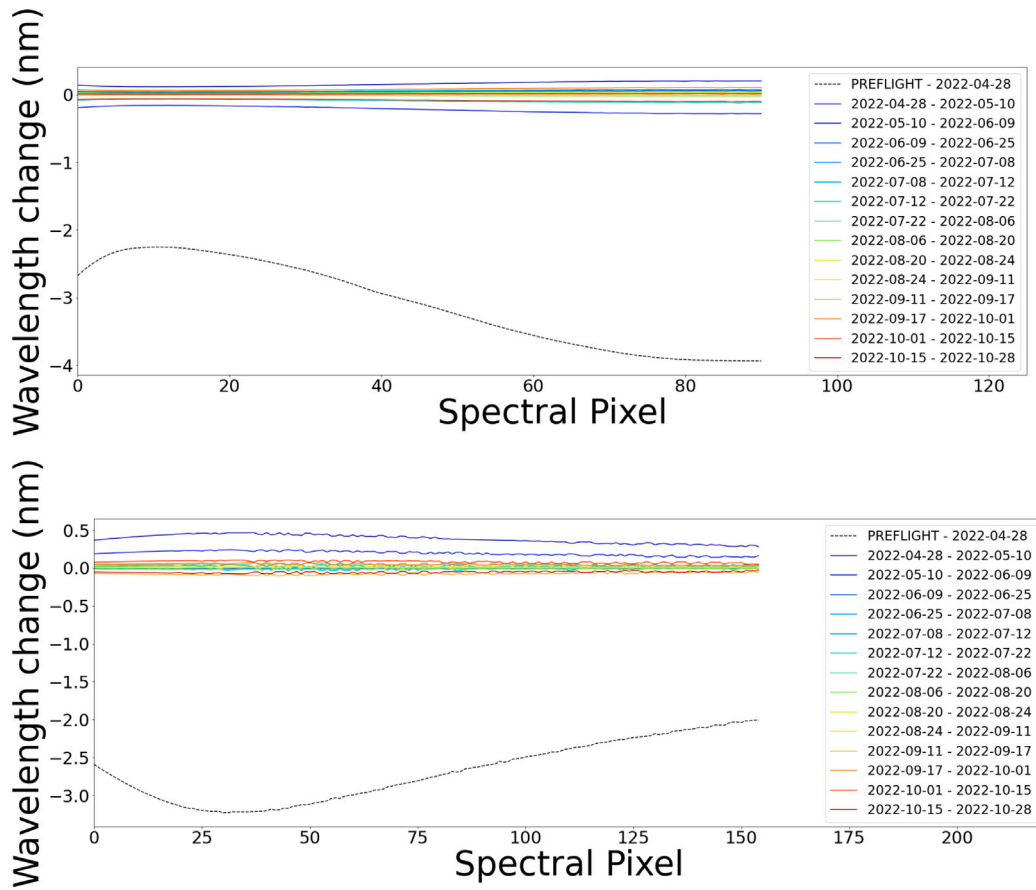
Fig. 3. Change in center wavelengths between consecutive calibration measurements for VNIR (top) and SWIR (bottom) including the change from pre-flight (black dashed line) to the first in-flight (blue solid line) spectral calibration (in nm).
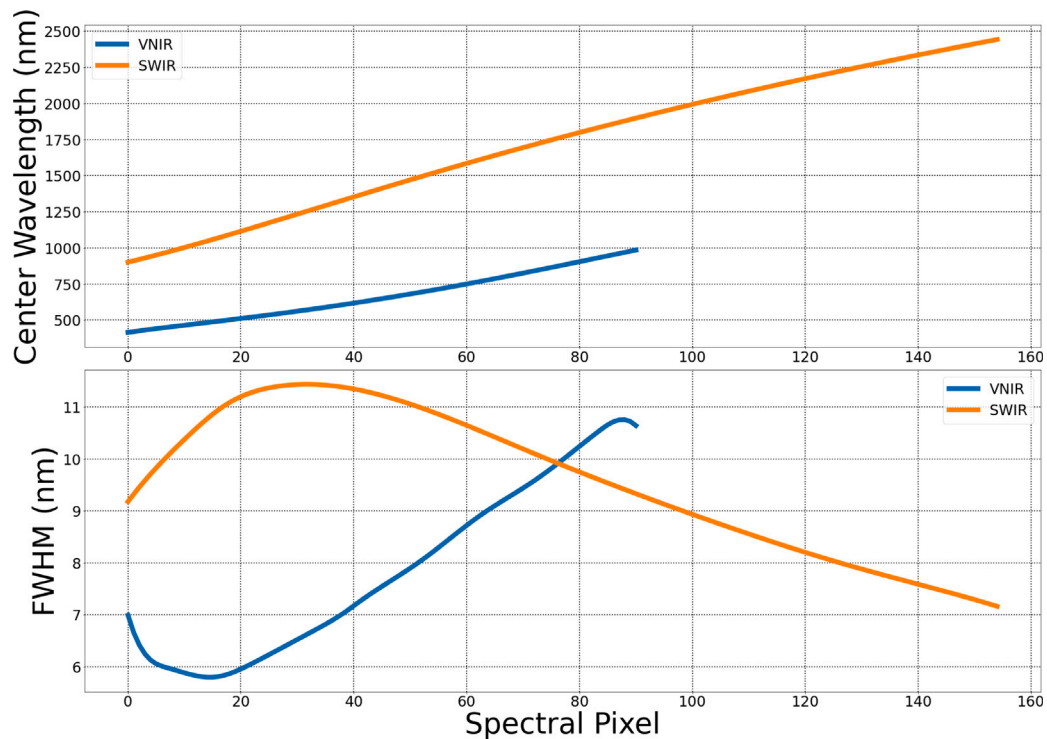

Fig. 4. Center wavelength (top) and full width at half maximum (bottom) in each spectral pixel/band of VNIR (91 pixels/bands) and SWIR (155 pixels/bands) (in nm).
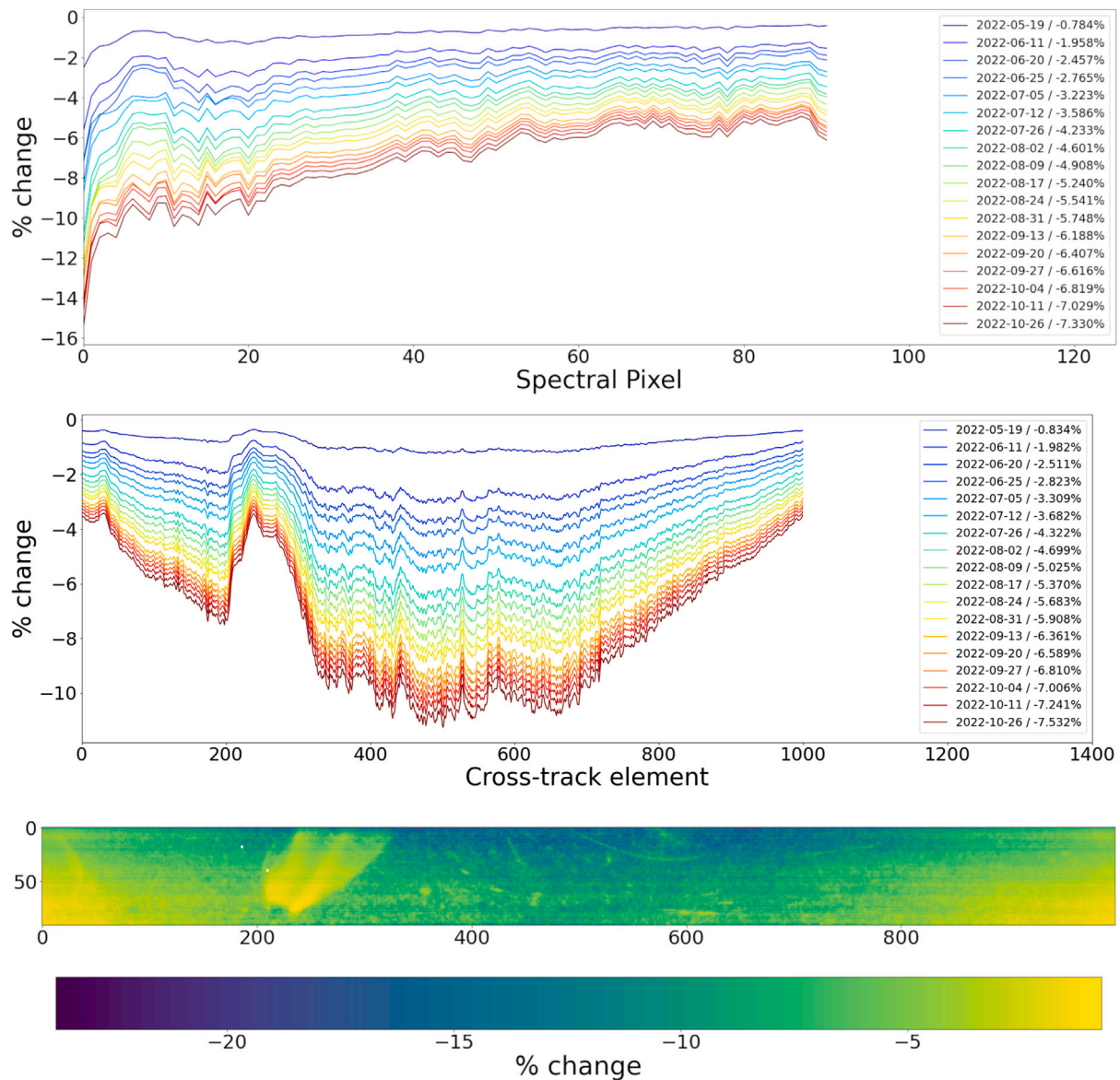
Fig. 5. Degradation in VNIR. Top: Percentage change relative to the first in-flight measurement averaged into spectral pixels/bands, total average given in legend per measurement. Middle: Percentage change relative to the first in-flight measurement averaged into spatial pixels, total average given in legend per measurement. Bottom: Percentage change from May 3rd, 2022, to October 26th, 2022, across the sensor.

are not accurate enough for absolute calibration. However, the fitted trend lines show a reduction of the degradation per day over time as illustrated in Fig. 6 and indicate that this effect will reach a negligible magnitude in March 2023. To mitigate for the current degradation, radiometric calibration tables have been issued every month based on the absolute radiometric calibration measurements. By the middle of 2023, the calibration coefficients will be modeled over time to further account for the degradation between calibration tables.

Relative radiometric measurements of SWIR show good stability over time, without any signs of degradation. Monitoring will nonetheless continue over the operational lifetime.

2.3.2. Absolute radiometric

Measurements of the Sun are taken in order to retrieve the absolute radiometric calibration coefficients (Storch et al., 2020). Due to the high radiation power of the Sun, a white Spectralon® diffusor with well-established properties is used and the high gain measurements are recorded at reduced integration times. With these measurements three kinds of coefficients are established for use in the radiometric processing:

- Radiometric calibration coefficients: the conversion factors between digital numbers and radiance, determined for each spectral band.
- Response Non-Uniformity (RNU) coefficients: a correction to account for radiometric pixel-to-pixel variations.
- Gain matching coefficients: a factor applied to the low gain measurements to match to the high gain levels, determined for each pixel.

The radiometric calibration coefficients are determined based on every Sun calibration which are taken at monthly intervals. Due to the degradation in the VNIR as described in Section 2.3.1, calibration tables have been updated on a monthly basis.

Immediately after launch, changes were observed in all coefficients. In the case of SWIR, the radiometric calibration coefficients changed by 3.5%, the RNU coefficients changed by 0.01% and the gain matching coefficients changed by 0.6%. Since this initial change, which was expected due to air–vacuum transition and gravity release, the SWIR coefficients have remained stable. In the case of VNIR, changes in the coefficients have continued to be observed owing to the ongoing
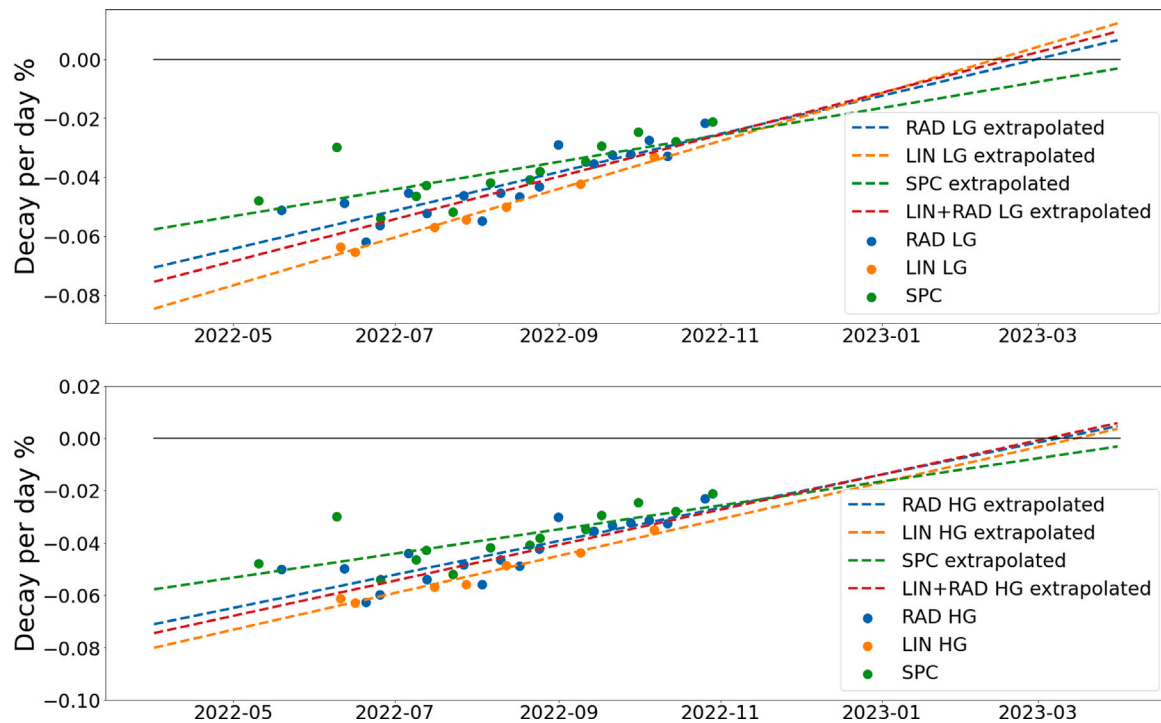
Fig. 6. Decay per day of the VNIR from the relative radiometric (RAD), linearity (LIN) and spectral (SPC) calibration measurements. Subsets of these data have been extrapolated into the future to model the degradation behavior.

degradation of the camera: until October 26th, 2022, the radiometric calibration coefficients had increased by 6.4% relative to the pre-flight tables and the RNU coefficients had generally increased by approx. 3% in the central pixels and decreased by more than 3% in the edge pixels. The behavior of the RNU coefficients is the inverse of the degradation map illustrated in the bottom of Fig. 5: where there is less degradation (e.g. on the sides), the RNU coefficients can be seen to decrease. Following an absolute post-launch change of 1% to 3%, the VNIR gain matching coefficients have remained stable, but the computation of the gain matching from the Sun observations for the higher wavelengths is affected by low signal values, where the linearity behavior is less well constrained (see Supplements.9 for details).

2.3.3. Linearity

The non-linear behavior of the sensors are characterized using dedicated LEDs (Light Emitting Diodes) in front of the Focal Plane Assembly (FPA). In VNIR, the LEDs have peak emission at 470 nm whilst in SWIR, the LEDs have peak emission at 1300 nm. The sensors are illuminated by the stable light source and measurements are made with increasing integration times which enable low and saturated radiance levels to be collected. The received flux is proportional to the integration time.

These calibration measurements are made at monthly intervals and the linearity behavior calculated in-flight is compared to pre-flight behavior. This analysis showed slight changes in the linearity with respect to integration time, but the overall correction remained similar and no significant deviations from pre-flight behavior have been noticed during the CP. As a result, no updates have been necessary. The Signal-to-Noise Ratio (SNR) is also derived from the non-linearity measurements. This is not a perfect set up for the assessment as the non-linearity measurements only cover a single wavelength and light level at increasing integration times. However, it is well constrained, covering a wide range of radiance including the levels of the solar reference spectrum. The SNR fulfills the requirement of 500:1 at 495 nm and 150:1 at 2200 nm.

2.3.4. Dark shutter and deep space

All EO acquisitions and calibration measurements begin and end with a series of dark value measurements, where the shutter calibration mechanism is closed, in order to correct for dark signals. As a result, there is an additional thermal emission contribution from the closed shutter which will have an effect in SWIR. Long-term monitoring during the CP has shown no significant changes in the dark value measurements or the deep space measurements, that are performed monthly, in comparison to pre-flight values. In fact, the comparison between the dark value and deep space measurements show negligible contributions in SWIR from the closed shutter which demonstrates that the instrument has good thermal control.

2.4. Geometric calibration

Geometric in-flight calibration is based on pre-flight calibration and simulations (Schwind et al., 2012) and regular EO acquisitions are used. For the pre-flight calibration, an extensive laboratory measurement campaign was performed to determine the alignment of all components. It comprises instrument to star sensors alignment, namely instrument boresight, and look angles or Line-Of-Sight (LOS) vectors of individual pixels, namely pixel boresight. Both types of measurements were performed while all performance relevant temperatures were within their tolerances. For the in-flight calibration, Ground Control Points (GCPs) are generated using image matching techniques with the EnMAP EO acquisition and a reference image database created from publicly available Sentinel-2 orthoimages (Drusch et al., 2012) and the publicly available global Copernicus DEM (Digital Elevation Model) at 30 m spatial resolution (Cenci et al., 2022). The geometric sensor model parameters are updated using a least-squares adjustment. Due to challenges in the measurement of attitude data during most of the CP, the first geometric calibration was performed in October 2022 and is valid for EO acquisitions acquired after November 1st, 2022. First results show a significant improvement in the VNIR-to-SWIR co-registration accuracy from approx. 0.9 pixels before the calibration to approx. 0.4 pixels after the calibration. The spatial VNIR-to-SWIR co-registration is expected to be further improved with the next geometric calibration which is planned for the beginning of 2023.

3. Processors, data quality assessment and independent product validation of Level 1B, Level 1C and Level 2A

3.1. Overview

The fully-automatic processing chain generates image products at three processing levels and to a user selected format, namely image data in BSQ, BIL, BIP, JPEG2000, or GeoTIFF and metadata in XML, which are then disseminated through web-based user interfaces based on archived Level 0 (L0) products as described in Section 1.4. For all processing levels the inclusion of procedures for generating per-pixel quality information and rich metadata is an integral part and was detailed during the evolution of the mission (Storch et al., 2018a).

The quality of all products is ensured by including automated online quality control routines in all processors and by establishing the offline analysis of selected products at all three processing levels over the entire operational lifetime. During the processing steps, rich metadata and per-pixel quality layers are generated and provided with each product to the user. All products are INSPIRE, ISO 19115-2 and ISO 19119 conform, and – in case of the L2A products over land – fulfill the CEOS (Committee on Earth Observation Satellites) ARD (Analysis Ready Data) for Land (CARD4L) specifications (Bachmann et al., 2021).

Additionally, the radiometric (TOA and BOA), geometric and general quality of the products of all three processing levels delivered to the users are independently and intensively validated by the EnMAP Science Segment with the support of international in-situ validation teams during the CP. The community's strong support led to excellent results. Compared to the calibration and data quality assessment efforts, the focus of the independent product validation is on in-situ measurements and methods driven by tiles of EO acquisitions to cover a user-related perspective (Brell et al., 2021). During the CP, intensive in-situ- and image-based validation activities covered different surface types including soil, vegetation, snow and water, different brightness and elevation levels as well as atmospheric conditions. To make a reasonably reliable statement regarding the product quality, 98 tiles were analyzed: 54 L1B, 46 L1C and 10 L2A.

It is important to note that all identified aspects in the next sections, which are identified for improvement during the routine operations, are already under consideration at calibration and processor level.

3.2. Chain

In order to generate the archive products and three different processing levels of user products, there are five processors (L0, L1B, L1C, L2A, and the output processor) and two processing chains (L0, LX). To create L0 masks and metadata containing information concerning the three possible LX products, all five processors are executed in sequence in the L0 processing chain. For the creation of any of the higher-level products, all processors, except the L0 processor, are executed in the LX processing chain.

The L0 product with a size of 1024 × 1024 pixels is always generated for long-term archiving in the product library, having attached the complete set of metadata and quality layers generated by the L1B, L1C and L2A processors, with their detailed Algorithm Theoretical Baseline Documents (ATBDs) available at EnMAP.org (2022). In this way, compliance with CARD4L specifications is ensured. The L1B, L1C and L2A products are generated by the processors on user request, with their product format specifications available at EnMAP.org (2022), and are not archived, but available to the user.

3.3. Level 1B

3.3.1. Processor

The L1B processor is responsible for the correction of the raw instrument data to at-sensor radiance, thereby collecting important quality indicators and interpolating the defective pixels, dead pixels or abnormal pixels identified by quality control. It takes as input the L0 products, image data and metadata corresponding to one tile of an EO acquisition, and a set of calibration tables. The processor is divided into two distinct sub-processors, namely L1B_rad for the radiometric calibration and data quality checks and L1B_int for the interpolation of defective pixels.

The L1B_rad sub-processor calibrates the raw instrument data based on a set of calibration tables suitable for the EO acquisition date and time. The sequential corrections steps are applied separately for VNIR and SWIR and include line offset correction (VNIR only), electronic offset correction (SWIR only), non-linearity correction, dark signal and digital offset correction, RNU correction, gain matching (low gain only), straylight correction, radiometric calibration and spectral referencing. Data quality indicators are collected during L1B_rad both at raw and calibrated image levels, allowing the CARD4L specifications to be fulfilled. These include per-pixel flags for saturation, artifacts, interpolation and an overall quality rating as well as rich metadata.

The L1B_int sub-processor identifies and flags defective pixels for interpolation during the calibration processing and during the online data quality checks. The interpolation of defective pixels is conducted in the spectral dimension on intermediate BOA reflectance spectra based on the original TOA radiance, obtained by a simplified atmospheric correction. This is done due to the smoothness of BOA reflectance spectra, which has a positive influence on the overall accuracy of the interpolation process. After interpolation, the atmospheric correction process is inverted resulting in interpolated TOA radiance.

The final output of the processor consists of two at-sensor radiance image cubes in sensor geometry, namely one for VNIR and one for SWIR, as well as associated metadata, quicklooks and masks. The cubes have 1024 along-track pixels, 1000 across-track pixels, and 91 and 133 spectral bands for VNIR and SWIR. Bands in the strong atmospheric absorption from 1391 nm to 1461 nm and from 1760 nm to 1939 nm are not transmitted and thus are not present in L1B products. Minor changes of these wavelength ranges are planned for investigation during the first half of 2023. The across-track pixels at the edges of the detectors are discarded as they are not illuminated, but used for monitoring of the dark signal. The L1B product serves as input to the geometric correction performed at L1C in the processing chain. In addition, the L1B product is also the starting point for specialized users interested in performing their own geometric or atmospheric corrections or for studying phenomena best observed in at-sensor radiance spectra like emitted radiation or atmospheric effects.

3.3.2. Data quality assessment and independent product validation

To support the data quality assessment, the calibrated radiance values per detector element are averaged for each tile of EO acquisitions and archived as detector maps within the L0 products (Bachmann et al., 2018), thereby averaging out the differences in surface properties and random noise to a large degree.

Additionally, by the independent product validation, the following assessments were performed: analysis of the spectral smile effect and Spectral Response Function (SRF), TOA comparisons with in-situ measurements and investigations of spatially-coherent radiometric or striping artifacts.

3.3.3. Spectral accuracy and stability

The spectral stability is regularly checked using tiles of EO acquisitions based on narrow and stable atmospheric absorption features, as illustrated in Fig. 7. Based on the detector maps, the spectral properties of the tiles are routinely assessed for all acquired EO acquisitions having spatially and spectrally homogeneous radiance properties. As no smile correction is applied, the analysis shows the instrument characteristics over time. The smile effect is the variation of the center wavelength of a band per pixel with spatial position in across-track direction. At the wavelengths of stable atmospheric features, including the 760 nm Oxygen A band and 2060 nm CO_2 absorption, simulations
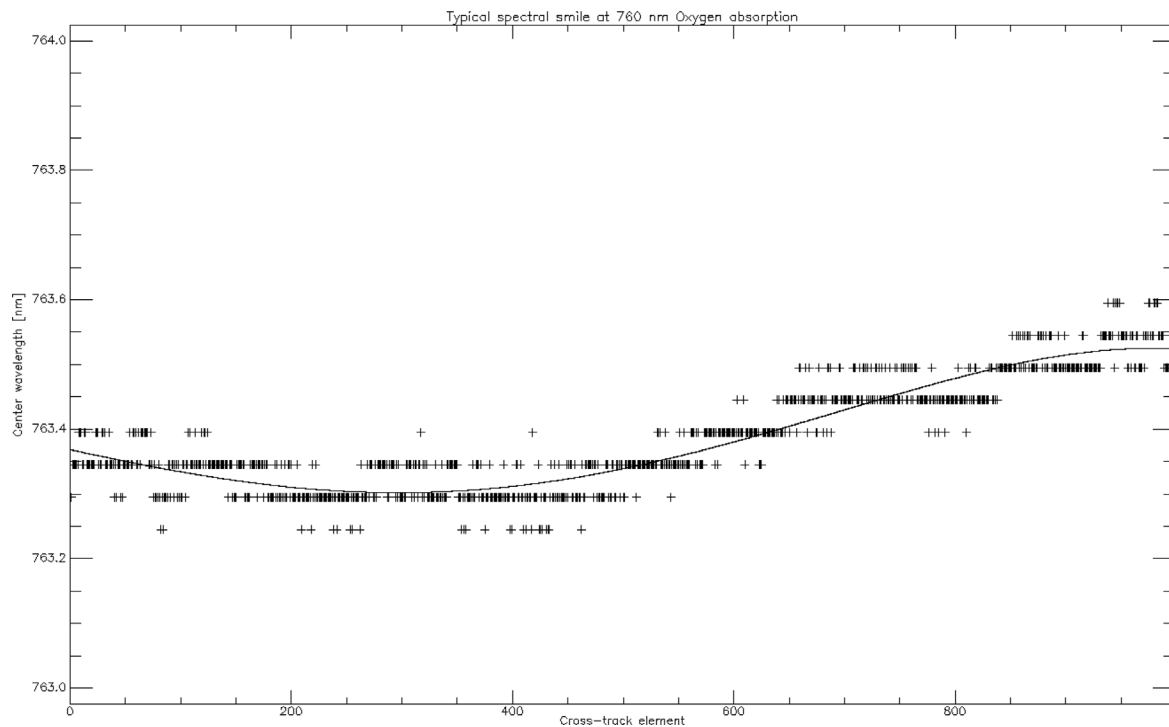
Fig. 7. Spectral smile at the 760 nm Oxygen A band absorption estimated using an EO acquisition. Crosses: center wavelength estimates for pixels. Line: fitted polynomial.

of spectral shifts were carried out by resampling the absorption in the interval of ± 3.0 nm with steps of 0.05 nm. The signal of the detector maps and the simulated shifted absorption were then normalized, and a least-square fit was used where the sensed absorption matches the simulations to thus estimate the center wavelength per across-track element. An additional polynomial fit was applied, as the CO_2 absorption band region in particular has low signals and is thus influenced by noise. When repeating this analysis for many detector maps, the spectral behavior over time is addressed. One important property is the standard deviation of the shift as this represents the spectral stability within the given period. At 760 nm it is better than 0.026% corresponding to 0.2 nm for all across-track elements and better than 0.029% corresponding to 0.6 nm at 2060 nm, for 1σ level (see Supplements.8 for details).

In addition, the across-track shape, namely the shape of the spectral smile, shows little variation. In case of VNIR, the stability is equally good for all across-track elements, while for SWIR the shape is similar to the detected center wavelength deviation. For the 760 nm Oxygen A band absorption, which is largely independent of other atmospheric influences, this estimated stability agrees well with the findings of the spectral calibration, while for the CO_2 feature the variability estimated vicariously is larger than it was based on the spectral calibration likely due to the lower Signal-to-Noise Ratio (SNR) and the general uncertainty of the vicarious estimation (see Supplements.7 for details). These findings result in typical uncertainties of the TOA and BOA products and updates previous analysis by Bachmann et al. (2015).

For the validation, the instrument Spectral Response Function (SRF), modeled as center wavelength and full width at half maximum of a Gaussian, has been characterized for seven appropriate tiles of EO acquisitions through the modeling of atmospheric absorption features at 760 nm (Oxygen A band) and at 2300 nm (methane) (Guanter et al., 2009).

The estimates of across-track spectral position variations are relatively small for 760 nm (VNIR) and 2300 nm (SWIR). The across-track shape of the center wavelength shift and full width at half maximum curves is almost identical for all seven analyzed tiles. For VNIR and SWIR, the across-track amplitude of the estimated shift is approx.

0.3 nm and 1.0 nm which corresponds to a linear displacement of a spectral pixel of approx. 4.1% and approx. 12.5% and thus within the spectral requirement of less than 20%. The amplitude of the full width at half maximum change in across-track is for VNIR (760 nm) approx. 0.4 nm and for the SWIR (2300 nm) approx. 0.5 nm.

3.3.4. Radiometric accuracy

The radiometric accuracy was assessed with the TOA reflectance provided by RadCalNet (RadCalNet, 2022; Bouvet et al., 2019) for the sites in Railroad Valley, NV, USA; La Crau, France; and Gobabeb, Namibia. During the CP, it was possible to perform 13 EO acquisitions (6 at Railroad Valley, 1 at La Crau and 6 at Gobabeb) with tilt angles below 20 deg, acceptable weather conditions and coincident RadCalNet data. While for Railroad Valley there was up to 15% discrepancy and large variability between EnMAP and RadCalNet, for Gobabeb the differences were approximately within 5% for VNIR and SWIR. For La Crau, there appeared to be a significant degree of discrepancy, but with only one EO acquisition available it was not possible to draw definite conclusions. Overall, using all EO acquisitions available for the three sites, the ratio between EnMAP and RadCalNet TOA reflectance was estimated to be 1.02 ± 0.06 for VNIR and 1.07 ± 0.04 for SWIR at 1σ level (see Supplements.10 for details). The reported differences between EnMAP and RadCalNet data are not to be directly understood as an estimate of radiometric accuracy of EnMAP since they are presumably due to a mix of uncertainties in the reference data and instrument as well as path radiance and BRDF (Bidirectional Reflectance Distribution Function) effects. Note in particular that the TOA uncertainties reported by RadCalNet amount to 3% to 5% for the sites and considered dates and that EnMAP has a radiometric accuracy requirement of 5%.

Through the validation, the TOA radiance measured by EnMAP was assessed using a reflectance-based approach. Seven in-situ BOA reference reflectance spectra from five scientific field campaigns – Black Rock Playa Zero, NV, USA; Amiaz Plain and Makhtesh Ramon, Israel; Pinnacles, Australia; Heller Pearlshtien and Ben-Dor (2022) and Ong et al. (2017); and two RadCalNet sites (RadCalNet, 2022; Bouvet et al., 2019) Railroad Valley and Gobabeb – were measured simultaneously to an EnMAP EO acquisition. The in-situ measurements were propagated
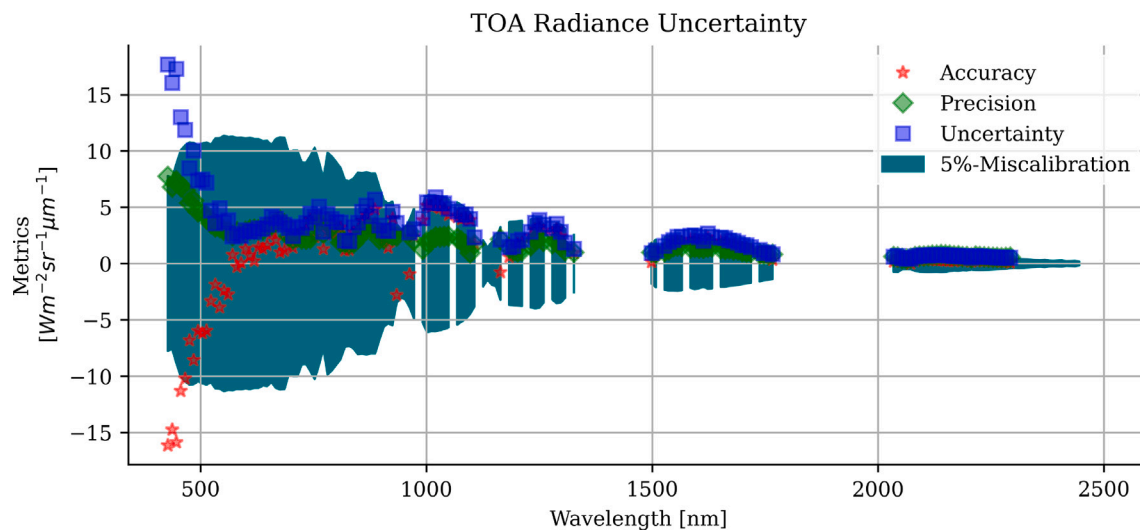
TOA Radiance Uncertainty

Fig. 8. Wavelength-dependent TOA radiance uncertainties for the seven comparisons. Accuracies (mean residual), precisions (standard deviation around mean measured values) and uncertainties (Root-Mean-Square Error) are plotted with the requirement of 5%-miscalibration.

to TOA radiance to compare and statistically analyze them with the TOA radiance measured by EnMAP. Based on strict quality criteria and investigation, adapted measurement procedures and iterative optimization of AOT and WV in the TOA propagation, the in-situ and propagation uncertainty budgets were ensured to be smaller than the radiometric requirement of 5%.

The uncertainties were stable within the radiometric requirement of 5% for most parts of the wavelength range as illustrated in Fig. 8. Only for the wavelength range between 400 nm and 450 nm were the uncertainties greater than the required 5%. Also, a slight tendency towards higher radiances for EnMAP compared to the in-situ data was identified for SWIR. Since suitable and reliable in-situ measurements and consistency with EnMAP EO acquisitions were limited during the CP, it is expected that more accurate and specific findings will be obtained based on different scenarios in 2023.

3.3.5. Radiometric stability

The radiometric stability was assessed over the well-known Pseudo-Invariant Calibration Sites (PICS) Algeria3, Lybia4 and Niger2 (CEOS, 2022; EROS, 2022). During the CP, it was possible to perform 14 EO acquisitions with tilt angles below 20 deg and acceptable weather conditions: 4 at Algeria3, 3 at Lybia4 and 7 at Niger2. The results in Fig. 9 illustrate that the calibrated radiance was stable over the whole period considered, especially for SWIR. Quantitatively, combining all the available EO acquisitions for the three sites, the deviation from the average TOA reflectance was around 2% for VNIR and 1% for SWIR at 1σ level. Given that in general the deviations are due to a combination of geometry of EO acquisition and instrument itself, it is feasible to conclude that EnMAP has a radiometric stability below 2% for VNIR and 1% for SWIR.

3.3.6. Fixed pattern noise and other striping artifacts

As EnMAP uses a CMOS (Complementary Metal-Oxide-Semiconductor) detector for VNIR, the bands at higher wavelengths are slightly affected by etaloning, also known as fringing, which was well characterized pre-flight (Baur et al., 2022). The effect, however, is small when compared to DESIS (Alonso et al., 2019) and other detectors based on CMOS.

During the CP, two sources of fixed pattern noise were identified, but both were within the relative and absolute radiometric accuracy of 2.5% and 5.0%. These sources cause visible striping artifacts in across-track dimension in the VNIR as well as minor along-track striping artifacts for some spectral bands in the SWIR.

First, small micro-vibrations of the SWIR cryocooler at a frequency of 44 Hz, which equate to an oscillation of approx. 5.2 frames, result in a small spectral instability. This introduces an along-track striping pattern in SWIR, but only bands with strong spectral gradients are affected. The effect on the calibrated radiance data are marginal but can be visualized (e.g. by principal component transformation) showing an along-track striping pattern every 5 ± 1 lines. Note, so far no impact on the LOS of the instrument has been detected due to these micro-vibrations.

Second, across-track striping artifacts occur in certain bands. For a detailed analysis a total of more than 2700 detector maps (excluding dead pixels) were compiled and split by the median overall radiance of the acquisition resulting in two groups of lower and higher radiance. They were then shifted by one pixel in across-track direction and the absolute difference was calculated per band. The overall radiance level is therefore not significant and only the change in across-track direction is relevant. The spatial variability of the Earth surface and random noise is largely reduced by the large number of detector maps, with the exception of bands at higher wavelengths in VNIR due to etalonging and for bands strongly affected by atmospheric absorption. The group with lower radiance shows a higher magnitude of pixel-to-pixel differences (approx. 0.4%) than the group with higher radiance (approx. 0.2%), indicating the relative small magnitude of this striping.

To summarize, fixed pattern noise and other striping artifacts are within the requirements. As the signal decreases, the additive nature of the phenomenon is relatively high, resulting in more prominent striping. Therefore, by the middle of 2023, changes in calibration and data processing will be investigated to further improve the image quality concerning these two effects.

Through the validation, across-track striping patterns inside L1B products and thus also in L1C and L2A products were investigated based on 54 tiles of EO acquisitions. Slight band- and column-wise deviations from a perfect sensor were detected for VNIR and SWIR but much smaller than 5%. Despite the low intensity, these striping anomalies affect further quantitative scientific processing and are suggested to be improved as planned. Also, along-track artifacts in SWIR caused by well-known micro-vibrations were detected and quantified. The analysis showed that the along-track anomalies occur only in wavelength ranges with a strong spectral gradient with a maximum amplitude for the anomaly of approx. 0.04%.

3.3.7. Dynamic range and blooming properties

The instrument performance at high radiance levels was assessed. The sensed radiance levels surpass the pre-flight threshold based on the
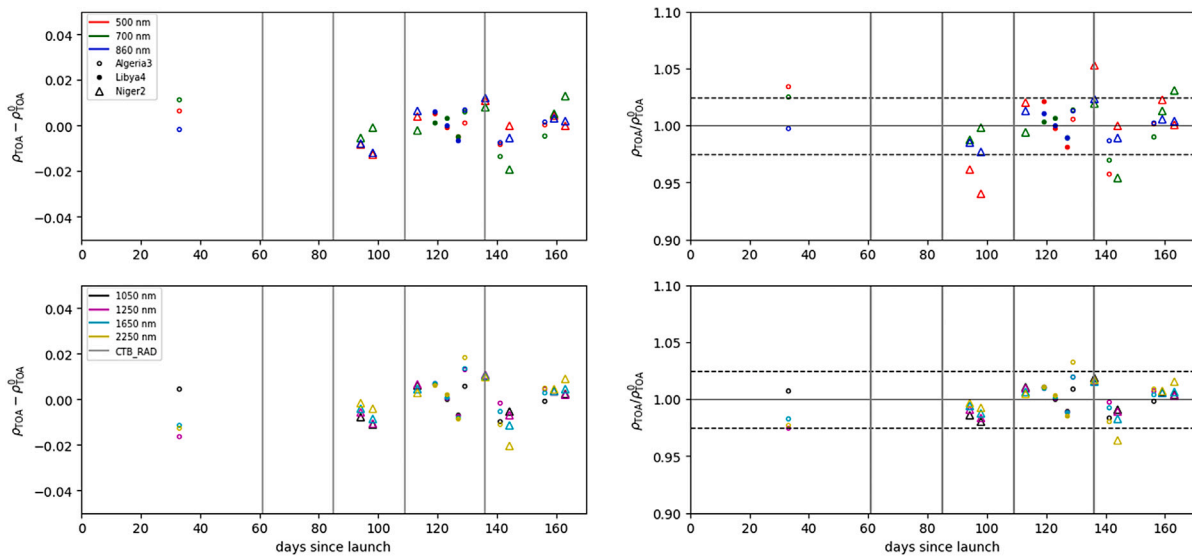
Fig. 9. Comparison between tile-averaged EnMAP TOA reflectance ρ_{TOA} and the average of all EO acquisitions ρ_{TOA}^0 in terms of absolute differences (left) and relative differences (right) at selected VNIR (top) and SWIR (bottom) wavelengths for EO acquisitions of the PICS sites Algeria3, Lybia4 and Niger2. Vertical lines mark the validity dates of radiometric calibration tables.

full well capacity of the detectors per band. Thereby the non-linearity at high radiance is also accounted for, demonstrating the dynamic range of the instrument. However, these pixels are flagged as saturated in the quality layers and metadata, because of the mentioned non-linearity at high radiance. Finally, blooming properties are checked, namely the ability of saturated pixels to influence the surrounding spatial pixels with normal radiance. Based on pre-flight assessments this was expected in some situations for SWIR and for the frame after the saturation, and is therefore also flagged as saturated. However, for all analyzed tiles of EO acquisitions, the frame after the saturation, as well as the frame before and the spatial pixels left and right do not show an abnormal behavior for VNIR or SWIR.

3.4. Level 1C

3.4.1. Processor

The L1C processor generates orthoimages employing the technique of the rigorous model of Direct Georeferencing (Müller et al., 2005). Orbit and attitude data measured with a frequency of 1 Hz are used as input as well as the sensor internal geometry of the instrument, which was extensively characterized pre-flight by highly accurate measurements. This also includes the geometric keystone effect.

An improvement of the sensor model is achieved by GCPs (Ground Control Points), which are extracted automatically using image matching techniques from a reference image database generated for the processor using Sentinel-2 orthoimages. In a first step tie points between the uncorrected image, where all tiles of an EO acquisition are considered, and a reference image are determined by an intensity-based matching. The tie points are complemented with interpolated Copernicus DEM height values and split up in GCPs and ICPs (Independent Check Points) based on quality criteria and distribution over the EO acquisition. In the next step, the sets of GCPs serve as input to improve the LOS model parameters within a least-squares adjustment process. Different levels of GCP outlier detection are included in the matching processes itself as well as in the least-squares adjustment of LOS model parameters. The ICPs are not used in this estimation, but to assess the geometric accuracy.

For the image orthorectification the DEM is used and light aberration and refraction are considered. Finally, a user selectable map projection system can be chosen, namely UTM (Universal Transverse Mercator) with the zone derived from the center coordinates of the EO

acquisition as well as the neighboring zones, geographic projection and the European LAEA (Lambert Azimuthal Equal-Area) projection. Within the map projection system image resampling is performed toward 30 m pixel spacing in case of UTM and European LAEA and 1 arcsec in case of geographic projection. Different selectable resampling methods to generate the final orthorectified products are offered to the user, namely nearest neighbor, bi-linear and cubic convolution. The L1C product also serves as input to the atmospheric compensation performed at L2A in the processing chain.

3.4.2. Data quality assessment and independent product validation

More than 1800 EO acquisitions were considered for geometric quality control. For approx. 1000 of those EO acquisitions (approx. 55%) enough GCPs and ICPs were identified for the geometric accuracy assessment including the spatial VNIR-to-SWIR co-registration.

Additionally, by the independent product validation, the following assessments were performed: analysis of the absolute spatial accuracy, the co-registration between VNIR and SWIR bands and the geometric keystone effect or spatial across-track distortions.

3.4.3. Geometric accuracy

The EO acquisitions without enough GCPs were not assessed quantitatively, but a random subset of them was inspected visually. The vast majority of those EO acquisitions were either almost fully covered with clouds or showed only water, desert, or rain forest. The behavior is thus as expected. Furthermore, a few EO acquisitions where less than 10 GCP were identified in total were inspected in detail. For most of those, no ICPs were identified, so no accuracy assessment could be performed. However, the few GCPs were used to modify the instrument boresight during the processing. The instrument boresight angles are close to the ones estimated for EO acquisitions with many more GCPs, so it is reasonable to assume that even with few GCPs, the geometric accuracy is sufficient. Only one EO acquisition was discovered where the low number of three available GCPs caused a challenge when generating the instrument boresight. To avoid this effect in the future, the processor was modified with a rough plausibility check of the resulting instrument boresight.

The assessment of the RMSE (Root-Mean-Square Error) values in the metadata illustrates that in x-direction, approx. 13% of the EO acquisitions are above 30 m, whereas in y-direction, approx. 4% of the EO acquisitions are above this threshold (see Supplements.11 for

details). The time-frame where the RMSE values are significantly higher correlates with the time-frame where the processor had a bug in the determination of the RMSE values which was fixed and did not affect the product itself. Therefore, it is reasonable to assume that the RMSE values for the affected EO acquisitions are in the range of those from the unaffected ones. When excluding the affected EO acquisitions, the percentage of EO acquisitions exceeding RMSE values of the required 30 m is approx. 3% in *x*-direction and approx. 2% in *y*-direction.

Through the validation, the absolute geometric accuracy was assessed using corresponding spatially high-resolution reference images of higher geometric accuracy. Spatially variable shifts between the L1C product and a reference are derived in the Fourier space using AROSICS (Automated and Robust Open-Source Image Co-registration Software, Scheffler et al., 2017). The RMSE in the *x*-direction with 17.43 m and *y*-direction with 19.29 m are both within the geometric requirement of 30 m.

3.4.4. Spatial VNIR-to-SWIR co-registration

It is important to note that VNIR and SWIR are not spatially aligned, namely there is a shift of approx. 190 arcsec (900 μrad) along-track which corresponds to approx. 600 m on ground (Schneider et al., 2012). Therefore, VNIR and SWIR are independently orthorectified and finally merged to a consistent product, where a co-registration of approx. 0.4 pixels was achieved at the end of the CP. The requirement of 0.3 pixels is violated and improvements will be investigated by the beginning of 2023.

Through the validation, the spatial variable shifts between the spectral overlapping VNIR (at 961.9 nm) and SWIR (at 968.6 nm) bands were derived based on cross-correlation in the Fourier space using AROSICS (Automated and Robust Open-Source Image Co-registration Software). The RMSE in the *x*-direction of 23.46 m and *y*-direction of 20.08 m did not meet the geometric requirement of less than 30% of a pixel and are suggested to be improved as planned.

3.4.5. Geometric keystone effect or spatial across-track distortions

Through the validation, the band-to-band across-track spatial misregistration caused by non-uniformity projection to the detector array, namely the geometric keystone effect, was assessed based on 36 suitable tiles of EO acquisitions. The algorithm detects across-track shifts based on cross-correlation in the Fourier space between consecutive bands using AROSICS (Automated and Robust Open-Source Image Co-registration Software). The validation of the keystone for VNIR and SWIR indicates a slight maximum across-track shift accumulated along bands of −0.072 pixels for VNIR and −0.081 pixels for SWIR. The inner across-track amplitude for the single bands is also negligibly small. Both sensors are well within the geometric requirement of less than 20% linear displacement of a spatial pixel.

3.5. Level 2A

3.5.1. Processor

The L2A processor consists of two individual sub-processors for the atmospheric correction of orthorectified TOA radiance over land and water surfaces. The underlying algorithms are PACO (Python-based Atmospheric COrrection, de los Reyes et al., 2020) and MIP (Modular Inversion Program, Kiselev et al., 2015). This enables the users to order L2A products for land and water separately or as a combined product featuring the results of both processors. Both processors consider, beside estimations of Aerosol Optical Thickness at 550 nm (AOT) and Water Vapor (WV), the adjacency effects and correct for cirrus, if requested by the user. Therefore, a classification (e.g. land–water–background, cloud) is performed. The land processor provides the BOA surface irradiance reflectance over both land and water pixels. The water processor considers water pixels only, where two distinctive products are available: sub-surface irradiance reflectance and normalized water-leaving reflectance. The masks in the quality layers are the same for all the products since they include the classification from the land and water processor.

3.5.2. Land processor

As a first processing step, masks are generated, in particular the land–water mask per pixel according to the spectrum, but also pixel classifications such as shadow, cloud, cirrus and haze with values none, thin, medium and thick. The haze correction is also performed in the land processor.

The land processor corrects for the atmospheric effects over tiles under flat or mountainous terrain to retrieve the reflectance of each pixel. AOT and WV are estimated per pixel and used to determine the radiative transfer functions, where the solar spectral irradiance model of Fontenla et al. (2011) is applied which is also considered for radiometric calibration to ensure consistency. Furthermore, information on the season (Wan, 2014) and Ozone (Platnick et al., 2016) using external databases is used. The correction of the topographic effects is performed using the DEM. It is applied by default unless it is excluded by the user or when less than 1% of the pixels have slope values greater than 6.0 deg which avoids artifacts due to noise in the DEM for tiles with a flat terrain (see EnMAP.org, 2022, for definitions in the L2A land algorithm theoretical baseline document).

3.5.3. Water processor

As a first processing step, the internal pixel classification mask as produced by the land processor is refined by the water processor regarding possible misclassification of water spectra and a Sun glint map by identification of specular reflection is added. Land class pixels that are considered as water pixels are accordingly changed and atmospherically corrected later.

Accounting for AOT estimated per water pixel, TOA radiance over water is transformed to BOA reflectance either as subsurface irradiance reflectance, which is the ratio between up-welling and down-welling irradiance just below the water surface, or as normalized water-leaving reflectance, which is the up-welling radiance under the consideration of Earth without an atmosphere, namely normalized or divided by down-welling solar irradiance, and considering an observation of the water body in nadir position with the Sun in zenith (see EnMAP.org, 2022, for definitions in the L2A water algorithm theoretical baseline document).

3.5.4. Data quality assessment and independent product validation

Through the validation, the cloud and cloud shadow masks were assessed for five tiles of EO acquisitions based on visual inspection. This indicated a slight underestimation of 1% to 8% for all investigated tiles and all cloud types. Also, false positives for haze and cloud shadows, and false-negative, especially for thin clouds but also for cloud shadows, have been detected.

3.5.5. Land products

The atmospheric parameters AOT and WV, estimated over land pixels, were checked with respect to data from AERONET (AErosol RObotic NETwork) sites (AERONET, 2022) during the CP. Fig. 10 shows the scatter plots of the EnMAP retrieved land AOT (left) and WV (right) 9 km around the AERONET site versus the in-situ measurements. The error bars correspond to 1σ, the requirements for both AOT and WV. The AOT scatter plot only contains tiles with at least 5% of the pixels covered by Dark Dense Vegetation (DDV).

For the assessment of BOA reflectance, the same RadCalNet sites as used for L1B are considered. In particular, Fig. 11 illustrates the uncertainty between EnMAP with tilt angles below 10 deg at Gobabeb and in-situ surface reflectance. Due to its arid nature, the site does not contain dark dense vegetation surfaces from which to estimate the AOT. The default AOT used in this type of tile resulted in a larger bias, especially when the atmosphere is as clear as it happens to be for this site. For a more reliable estimation of the atmospheric correction performance, the in-situ measurements of AOT were forced to be used by the processor.

The same processor is capable of correcting for the atmospheric effects for other missions like Sentinel-2, here B unit, and Landsat-9.
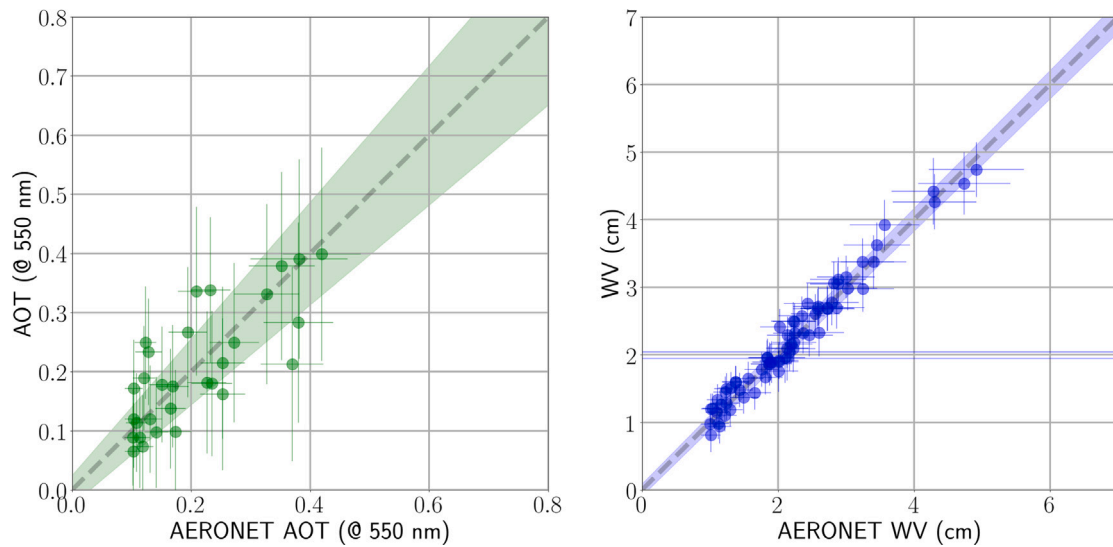
Fig. 10. EnMAP land AOT (unitless; left) and WV (in cm; right) versus the AERONET in-situ measurements. Shadowed area: EnMAP uncertainties of required 1σ.
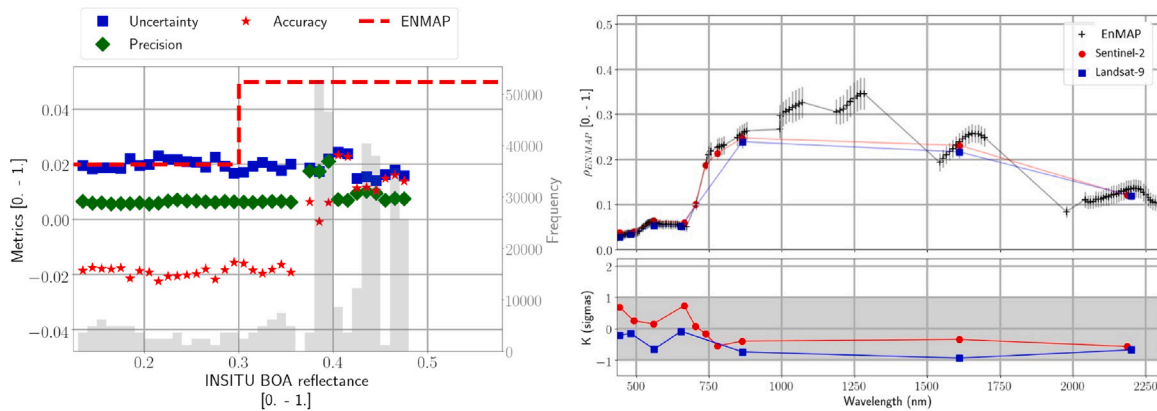

Fig. 11. Left: Uncertainty (blue squares), precision (green diamonds) and accuracy (red stars) of EnMAP EO acquisitions at Gobabeb versus reference in-situ reflectance. Dashed red line: EnMAP requirement. Gray histogram: frequency or amount of reference pixels considered in the validation for each in-situ reflectance bin. Right: EnMAP (black pluses), Sentinel-2 (red circles) and Landsat-9 (blue squares) BOA reflectance during the passes at the AERONET site of Sioux Falls. The bottom plot shows the coverage factor of the spectral difference between EnMAP spectra and Sentinel-2 (red circles) and Landsat-9 (blue squares) with respect to the expanded uncertainty of each pair of spectra. The shadow gray area corresponds to $K = \pm 1$.

Fig. 11 illustrates the atmospheric corrected results for a pass of En-MAP, Sentinel-2 and Landsat-9 at the AERONET site of Sioux Falls, SD, USA, on August 30th, 2022. The site has enough dark dense vegetation to provide information to estimate the AOT. In addition, AOT in-situ measurements of AERONET were verified to be within the requirements for the three observations, separated by less than one hour.

Through the validation, the BOA reflectance over land was assessed based on ten in-situ spectral reference measurements: Black Rock Playa; Amiaz Plain and Makhtesh Ramon; Pinnacles; Barrax and Camarena, Spain; Berlin-Tegel and Munich-Isar, Germany (Heller Pearlshtien and Ben-Dor, 2022; Ong et al., 2017); and three sites of RadCalNet (RadCal-Net, 2022; Bouvet et al., 2019) Railroad Valley, La Crau and Gobabeb. They were optimally measured close in time or concurrently to an EnMAP EO acquisition. The BOA reflectance over land validations were performed for tilt angles below 15 deg, variable albedo, elevation and atmosphere conditions and thus under representative EnMAP EO acquisition conditions.

The statistical assessment of BOA reflectance over land comparisons indicates that the requirements are generally fulfilled. Fig. 12 illustrates the level-dependent BOA reflectance statistics. For small reflectance levels, namely for less than 10%, which occur more frequently in the lower and higher wavelength domains, the uncertainties are larger

than 1%. For large reflectance levels, namely for at least 10%, it fits well below the accuracy requirements of 2% and 5%. The increased uncertainties between 400 nm and 550 nm and the small reflectance levels are due to the lack of aerosol influence compensation for EnMAP EO acquisitions without dark dense vegetation. To generate significant validation statistics, match-up of tiles of EO acquisitions without dark dense vegetation and assumed standard atmosphere had to be used in the analyzes during the CP.

3.5.6. Water products

AOT and normalized water-leaving reflectance as estimated for water pixels were checked with respect to AOT and normalized water-leaving radiance data as provided by in-situ measurements for AERONET-OC (AErosol RObotic NETwork-Ocean Color) sites (Zibordi et al., 2009).

AOT and reflectance measurements were considered under the nominal conditions of no Sun glint pollution of the considered pixels, clear water and a maximum time delta of half an hour between EnMAP pass and in-situ measurement. In order to enable comparisons of AERONET-OC radiance measurements with the derived reflectance for EnMAP, in-situ measurements were converted by multiplying by π and dividing by the solar model by Thuillier et al. (2003).
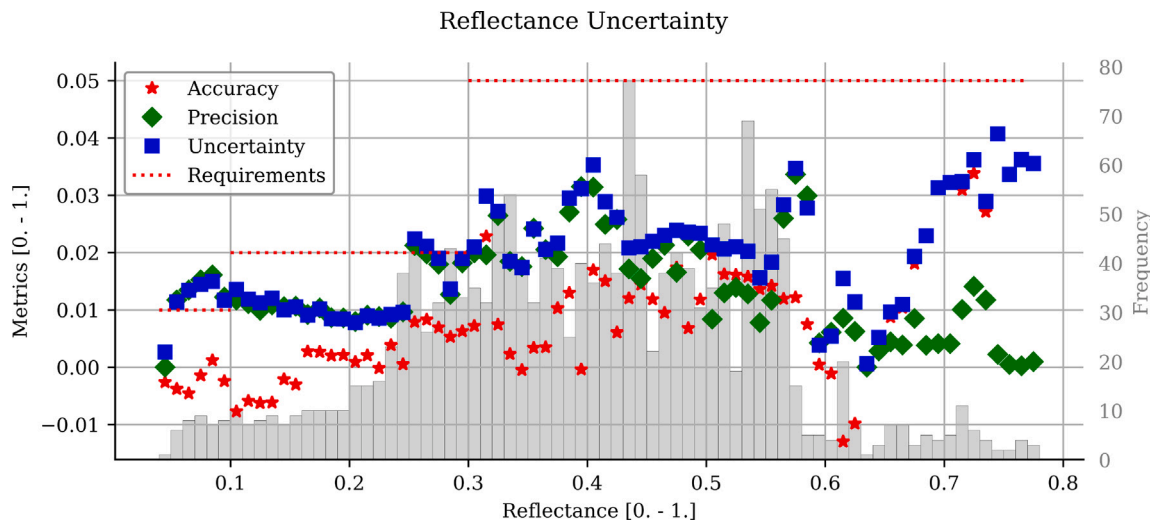
Fig. 12. Level-dependent BOA reflectance uncertainties for the ten comparisons. Accuracies (mean residual), precisions (standard deviation around mean measured values) and uncertainties (RMSE) are plotted with the requirement, namely < 0.01 for $\rho < 0.1$ and < 0.02 for $0.1 \leq \rho < 0.3$ and < 0.05 for $0.3 \leq \rho \leq 0.6$.
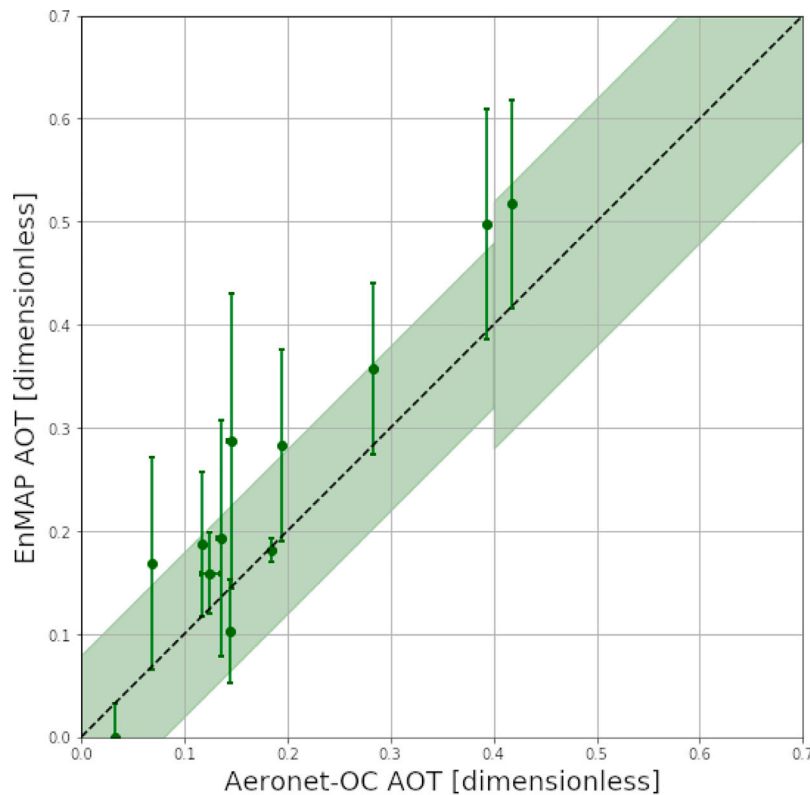

Fig. 13. EnMAP water AOT (unitless) versus AERONET-OC in-situ measurements for EO acquisitions under nominal conditions. Shadowed area: EnMAP uncertainties of required 1σ.

A total of 12 EO acquisitions featuring the nominal conditions were considered. Fig. 13 shows the scatter plots of the EnMAP retrieved water AOT 9 km around the AERONET-OC site versus the in-situ measurements. Fig. 14 displays two exemplary spectra at the AERONET-OC sites of the Galata Platform, Black Sea, and Bahia Blanca, Atlantic Ocean. Both AOT and reflectance measurements of the 12 EO acquisitions were verified to be within the requirements. The EnMAP water subsurface irradiance reflectance product was checked by means of conversion to normalized water-leaving reflectance due to the scarce availability of direct in-situ measurements and was checked to be within the requirements, too.

Through the validation, the BOA reflectance over water, namely the normalized water leaving reflectance product, was assessed based on in-situ spectral reference measurements at different coastal and inland water sites: Lake Constance, Germany, two hand-held measurements (Bracher et al., 2021); Lake Trasimeno, Italy, one fixed measurement (Bresciani et al., 2020); Lucinda Jetty Coastal Observatory, Australia, two fixed measurements (Schroeder et al., 2022; Soja-Woźniak et al., 2019); and Aqua Alta Oceanographic Tower, Italy, one fixed AERONET-OC (AERONET, 2022; Zibordi et al., 2009) and one fixed HYPERNETS measurement (HYPERNETS, 2022; Concha et al., 2021). They were optimally measured close in time or concurrently to an EnMAP EO
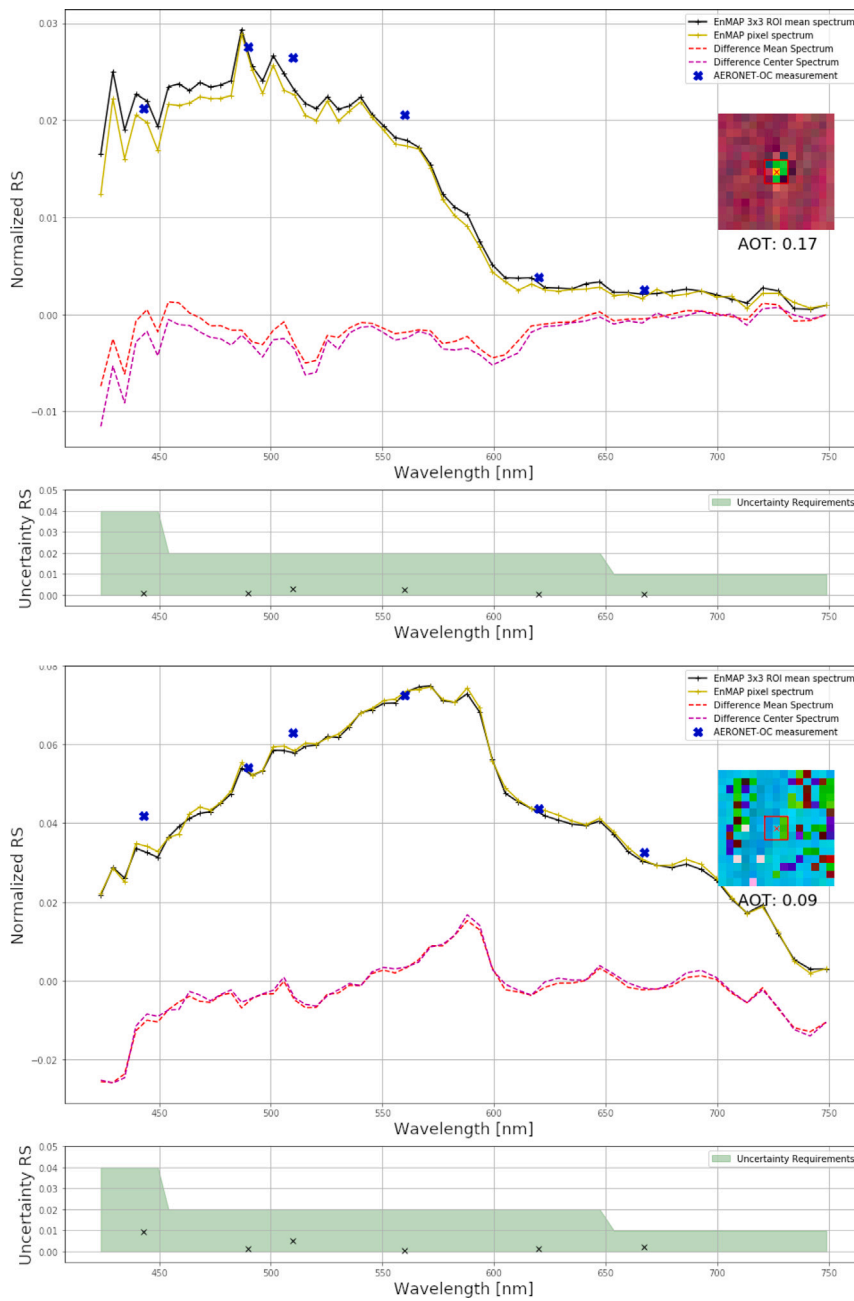
Fig. 14. EnMAP water normalized water-leaving reflectance versus AERONET-OC in-situ measurements. Top: Galata Platform. Bottom: Bahia Blanca. Yellow line: Spectrum of single EnMAP pixel at AERONET-OC site. Black line: Mean spectrum of 3 × 3 EnMAP pixel (Region-of-Interest (ROI)) at AERONET-OC site. Blue dots: Transformed AERONET-OC measurements. Dashed red and magenta lines: Per-band difference between EnMAP and AERONET-OC. Bottom: Uncertainty and EnMAP requirement, which are relative, namely not a function on the signal, but depend on the wavelength and AOT.

acquisition, namely quality-controlled match-ups are considered. The BOA reflectance over water validations were performed for tilt angles below 25 deg.

The statistical assessment of the BOA reflectance over water comparisons indicates that the requirements are generally fulfilled. Uncertainties are larger between 400 nm and 550 nm, but the accuracy requirements for six out of seven match-ups are fulfilled. The accuracy requirements when not considering ranges with strong atmospheric and for AOT less than 0.4 is: 0.04 for 400 nm $< \lambda \le$ 450 nm, 0.02 for 450 nm $< \lambda \le$ 650 nm and 0.01 for 650 nm $< \lambda \le$ 800 nm. For AOT larger than 0.4 the corresponding value increases by 0.01.

4. Conclusions

Between the launch of EnMAP on April 1st, 2022, and entering the routine operations on November 2nd, 2022, a large variety of activities and analyses were successfully executed to verify and validate the high performance of the high-resolution imaging spectroscopy remote sensing mission. The complete cycle of acquisition planning to product delivery is considered and expected improvements are illustrated including the usability of user interfaces, consideration of dynamic radiometric calibration coefficients and algorithms to mitigate striping effects. It has been illustrated that the spectral and radiometric

accuracy and stability is better than 0.5 nm and 2.5% between consecutive calibration measurements over the complete spectral range between 418.2 nm and 2445.5 nm with negligible smile effects. The geometric accuracy is better than 20 m, where the confirmed ground instantaneous field-of-view is 30 m × 30 m at a swath width of 30 km. A swath length of up to 5550 km is acquirable per day with negligible keystone effects and it is expected that the co-registration will further improve from 0.4 pixels to 0.1 pixels. Intensive data quality assessment and independent product validation efforts were successfully performed for all three released user product levels of the fully-automatic image processing chain, and will continue to be performed – and extended – during routine operations. Based on our detailed analysis, no major discrepancies with the requirements were identified and further improvements in performance are planned for 2023.

CRediT authorship contribution statement

Tobias Storch: Conceptualization, Methodology, Writing – original draft, Writing – review & editing (related to EnMAP Ground Segment), Funding acquisition, Supervision. **Hans-Peter Honold:** Writing – review & editing (related to EnMAP Space and Science Segment), Funding acquisition, Supervision. **Sabine Chabrillat:** Writing – review & editing (related to EnMAP Space and Science Segment), Funding acquisition, Supervision. **Martin Habermeyer:** Investigation, Writing – review & editing (related to EnMAP Ground and Space and Science Segment). **Paul Tucker:** Investigation, Writing – review & editing (related to EnMAP Ground and Space and Science Segment). **Maximilian Brell:** Investigation, Writing – review & editing (related to EnMAP Ground and Space and Science Segment). **Andreas Ohndorf:** Investigation, Writing – review & editing (related to EnMAP Ground and Space Segment with focus on platform). **Katrin Wirth:** Investigation, Writing – review & editing (related to EnMAP Ground and Space Segment with focus on platform). **Matthias Betz:** Investigation, Writing – review & editing (related to EnMAP Ground and Space Segment with focus on platform). **Michael Kuchler:** Investigation, Writing – review & editing (related to EnMAP Ground and Space Segment with focus on platform). **Helmut Mühle:** Investigation, Writing – review & editing (related to EnMAP Ground and Space Segment with focus on payload). **Emiliano Carmona:** Investigation, Writing – review & editing (related to EnMAP Ground and Space Segment with focus on payload). **Simon Baur:** Investigation, Writing – review & editing (related to EnMAP Ground and Space Segment with focus on payload). **Martin Mücke:** Investigation, Writing – review & editing (related to EnMAP Ground and Space Segment with focus on payload). **Sebastian Löw:** Software, Investigation, Writing – original draft (related to operations). **Daniel Schulze:** Software, Investigation, Writing – original draft (related to operations). **Steffen Zimmermann:** Software, Investigation, Writing – original draft (related to operations). **Christoph Lenzen:** Software, Investigation, Writing – original draft (related to operations). **Sebastian Wiesner:** Software, Investigation, Writing – original draft (related to operations). **Saika Aida:** Software, Investigation, Writing – original draft (related to orbit and attitude). **Ralph Kahle:** Software, Investigation, Writing – original draft (related to orbit and attitude). **Peter Willburger:** Software, Investigation, Writing – original draft (related to S- and X-band). **Sebastian Hartung:** Software, Investigation, Writing – original draft (related to S- and X-band). **Daniele Dietrich:** Software, Investigation, Writing – original draft (related to user interfaces to order product and acquisitions, processing and operations). **Nicolae Plesia:** Software, Investigation, Writing – original draft (related to user interfaces to order product and acquisitions, processing and operations). **Mirco Tegler:** Software, Investigation, Writing – original draft (related to user interfaces to order product and acquisitions, processing and operations). **Katharina Schork:** Software, Investigation, Writing – original draft (related to user interfaces to order product and acquisitions, processing and operations). **Kevin Alonso:** Software, Formal analysis, Writing – original draft (related to in-flight calibration and monitoring). **David Marshall:** Software, Formal analysis, Writing – original draft (related to in-flight calibration and monitoring). **Birgit Gerasch:** Software, Formal analysis, Writing – original draft (related to in-flight calibration and monitoring). **Peter Schwind:** Software, Formal analysis, Writing – original draft (related to processor chain, L1B, L1C, L2A land and water with contributions to data quality assessment). **Miguel Pato:** Software, Formal analysis, Writing – original draft (related to processor chain, L1B, L1C, L2A land and water with contributions to data quality assessment). **Mathias Schneider:** Software, Formal analysis, Writing – original draft (related to processor chain, L1B, L1C, L2A land and water with contributions to data quality assessment). **Raquel de los Reyes:** Software, Formal analysis, Writing – original draft (related to processor chain, L1B, L1C, L2A land and water with contributions to data quality assessment). **Maximilian Langheinrich:** Software, Formal analysis, Writing – original draft (related to processor chain, L1B, L1C, L2A land and water with contributions to data quality assessment). **Julian Wenzel:** Software, Formal analysis, Writing – original draft (related to processor chain, L1B, L1C, L2A land and water with contributions to data quality assessment). **Martin Bachmann:** Software, Formal analysis, Writing – original draft (related to data quality assessment with contributions to processor chain, L1B, L1C, L2A land and water). **Stefanie Holzwarth:** Software, Formal analysis, Writing – original draft (related to data quality assessment with contributions to processor chain, L1B, L1C, L2A land and water). **Nicole Pinnel:** Visualization, Writing – review & editing (related to EnMAP user interfaces). **Luis Guanter:** Software, Investigation, Writing – original draft (related to independent product validation). **Karl Segl:** Software, Investigation, Writing – original draft (related to independent product validation). **Daniel Scheffler:** Software, Investigation, Writing – original draft (related to independent product validation). **Saskia Foerster:** Software, Investigation, Writing – original draft (related to independent product validation). **Niklas Bohn:** Software, Investigation, Writing – original draft (related to independent product validation). **Astrid Bracher:** Software, Investigation, Writing – original draft (related to independent product validation). **Mariana A. Soppa:** Software, Investigation, Writing – original draft (related to independent product validation). **Ferran Gascon:** Software, Investigation, Writing – original draft (related to independent product validation). **Rob Green:** Software, Investigation, Writing – original draft (related to independent product validation). **Raymond Kokaly:** Software, Investigation, Writing – original draft (related to independent product validation). **Jose Moreno:** Software, Investigation, Writing – original draft (related to independent product validation). **Cindy Ong:** Software, Investigation, Writing – original draft (related to independent product validation). **Manuela Sornig:** Writing – review & editing (related to EnMAP Mission Management), Funding acquisition, Project administration. **Ricarda Wernitz:** Writing – review & editing (related to EnMAP Mission Management), Funding acquisition, Project administration. **Klaus Bagschik:** Writing – review & editing (related to EnMAP Mission Management), Funding acquisition, Project administration. **Detlef Reintsema:** Writing – review & editing (related to EnMAP Mission Management), Funding acquisition, Project administration. **Laura La Porta:** Writing – review & editing (related to EnMAP Mission Management), Funding acquisition, Project administration. **Anke Schickling:** Writing – review & editing (related to EnMAP Mission Management), Funding acquisition, Project administration. **Sebastian Fischer:** Writing – review & editing (related to EnMAP Mission Management), Funding acquisition, Project administration.

Declaration of competing interest

The authors declare that they have no known competing financial interests or personal relationships that could have appeared to influence the work reported in this paper.

Data availability

All EnMAP products are freely available from https://www.enmap.org/.

Acknowledgments

Appendix A. Supplementary data

Supplementary material related to this article can be found online at https://doi.org/10.1016/j.rse.2023.113632. It contains details on topics as referenced in the article by Supplements.Section.

References

AERONET, 2022. AErosol RObotic NETwork Portal. aeronet.gsfc.nasa.gov.

Alonso, K., Bachmann, M., Burch, K., Carmona, E., Cerra, D., de los Reyes, R., Dietrich, D., Heiden, U., Hölderlin, A., Ickes, J., Knodt, U., Krutz, D., Lester, H., Müller, R., Pagnutti, M., Reinartz, P., Richter, R., Ryan, R., Sebastian, I., Tegler, M., 2019. Data products, quality and validation of the DLR Earth Sensing Imaging Spectrometer (DESIS). Sensors 19 (20), 4471–4515. http://dx.doi.org/10.3390/s19204471.

Bachmann, M., Alonso, K., Carmona, E., Cerra, D., de los Reyes, R., Gerasch, B., Habermeyer, M., Krawczyk, H., Langheinrich, M., Müller, R., Palubinskas, G., Pato, M.F.V., Schneider, M., Schwind, P., Storch, T., Ziel, V., 2018. Procedures for DataQC within the EnMAP and DESIS ground segments. In: Proceedings of WHISPERS 2018.

Bachmann, M., Alonso, K., Carmona, E., Gerasch, B., Habermeyer, M., Holzwarth, S., Krawczyk, H., Langheinrich, M., Marshall, D., Pato, M., Pinnel, N., de losReyes, R., Schneider, M., Schwind, P., Storch, T., 2021. Analysis-Ready Data from hyperspectral sensors—The design of the EnMAP CARD4L-SR Data Product. Remote Sens. 13 (22), http://dx.doi.org/10.3390/rs13224536.

Bachmann, M., Makarau, A., Segl, K., Richter, R., 2015. Estimating the influence of spectral and radiometric calibration uncertainties on EnMAP data products—Examples for ground reflectance retrieval and vegetation indices. Remote Sens. 7 (8), 10689–10714. http://dx.doi.org/10.3390/rs70810689.

Barnes, W.L., Xiong, X., Salomonson, V.V., 2003. Status of Terra MODIS and Aqua MODIS. Adv. Space Res. 32 (11), 2099–2106. http://dx.doi.org/10.1016/S0273-1177(03)90529-1.

Baur, S., Mücke, M., Sang, B., Wachter, R., Lettner, M., Honold, H.-P., Sornig, M., Fischer, S., 2022. Pre-flight calibration and characterization of the EnMAP sensor. In: Proceedings of SPIE, International Conference on Space Optics 2022. ICSO.

Baur, S., Wachter, R., Basili, P., Lettner, M., Mücke, M., Sornig, M., Fischer, S., 2019. Calibration and characterization of the EnMAP hyperspectral imager. In: Proceedings of SPIE, Remote Sensing 2019, Sensors, Systems, and Next-Generation Satellites XXIII, Vol. 11151. pp. 265–272. http://dx.doi.org/10.1117/12.2532715.

Bouvet, M., Thome, K., Berthelot, B., Bialek, A., Czapla-Myers, J., Fox, N.P., Goryl, P., Henry, P., Ma, L., Marcq, S., Meygret, A., Wenny, B.N., Woolliams, E.R., 2019. RadCalNet: A Radiometric Calibration Network for Earth observing imagers operating in the visible to shortwave infrared spectral range. Remote Sens. 11 (20), http://dx.doi.org/10.3390/rs11202401.

Bracher, A., Soppa, M.A., Gege, P., Losa, S.N., Silva, B., Steinmetz, F., Dröscher, I., 2021. Extension of atmospheric correction polymer to hyperspectral sensors: Application to HICO and first results for DESIS data. In: Proceedings of 2021 IEEE International Geoscience and Remote Sensing Symposium. IGARSS, pp. 1237–1240. http://dx.doi.org/10.1109/IGARSS47720.2021.9553568.

Brell, M., Guanter, L., Segl, K., Scheffler, D., Bohn, N., Bracher, A., Soppa, M.A., Foerster, S., Storch, T., Bachmann, M., Chabrillat, S., 2021. The EnMAP satellite—Data product validation activities. In: Proceedings of WHISPERS 2021.

Bresciani, M., Pinardi, M., Free, G., Luciani, G., Ghebrehiwot, S., Laanen, M., Peters, S., Della Bella, V., Padula, R., Giardino, C., 2020. The use of multisource optical sensors to study phytoplankton spatio-temporal variation in a shallow turbid lake. Water 12 (1), http://dx.doi.org/10.3390/w12010284.

Celesti, M., Rast, M., Adams, J., Boccia, V., Gascon, F., Isola, C., Nieke, J., 2022. The Copernicus Hyperspectral Imaging Mission for the Environment (CHIME): Status and planning. In: Proceedings of 2022 IEEE International Geoscience and Remote Sensing Symposium. IGARSS, pp. 5011–5014. http://dx.doi.org/10.1109/IGARSS46834.2022.9883592.

Cenci, L., Galli, M., Santella, C., Boccia, V., Albinet, C., 2022. Analyzing the impact of the different instances of the Copernicus DEM dataset on the orthorectification of VHR optical data. In: Proceedings of 2022 IEEE International Geoscience and Remote Sensing Symposium. IGARSS, pp. 6001–6004. http://dx.doi.org/10.1109/IGARSS46834.2022.9884037.

CEOS, 2022. CEOS Cal/Val Portal. calvalportal.ceos.org/pics_sites.

Cogliati, S., Sarti, F., Chiarantini, L., Cosi, M., Lorusso, R., Lopinto, E., Miglietta, F., Genesio, L., Guanter, L., Damm, A., Pérez-López, S., Scheffler, D., Tagliabue, G., Panigada, C., Rascher, U., Dowling, T., Giardino, C., Colombo, R., 2021. The PRISMA imaging spectroscopy mission: overview and first performance analysis. Remote Sens. Environ. 262, http://dx.doi.org/10.1016/j.rse.2021.112499.

Concha, J.A., Bracaglia, M., Brando, V.E., 2021. Assessing the influence of different validation protocols on Ocean Colour match-up analyses. Remote Sens. Environ. 259, http://dx.doi.org/10.1016/j.rse.2021.112415.

Connelly, D.S., Thompson, D.R., Mahowald, N.M., Li, L., Carmon, N., Okin, G.S., Green, R.O., 2021. The EMIT mission information yield for mineral dust radiative forcing. Remote Sens. Environ. 258, http://dx.doi.org/10.1016/j.rse.2021.112380.

Damerow, H., Schwarz, J., Richter, J., Maass, H., 2010. Integrated real-time processing of X-band telemetry. In: Proceedings of European Telemetry Conference (etc) 2010. pp. 1–4.

Drusch, M., Del Bello, U., Carlier, S., Colin, O., Fernandez, V., Gascon, F., Hoersch, B., Isola, C., Laberinti, P., Martimort, P., et al., 2012. Sentinel-2: ESA's optical high-resolution mission for GMES operational services. Remote Sens. Environ. 120, 25–36. http://dx.doi.org/10.1016/j.rse.2011.11.026.

Drusch, M., Moreno, J., Del Bello, U., Franco, R., Goulas, Y., Huth, A., Kraft, S., Middleton, E.M., Miglietta, F., Mohammed, G., Nedbal, L., Rascher, U., Schüttemeyer, D., Verhoef, W., 2017. The FLuorescence EXplorer mission concept—ESA's earth explorer 8. IEEE Trans. Geosci. Remote Sens. 55 (3), 1273–1284. http://dx.doi.org/10.1109/TGRS.2016.2621820.

EnMAP.org, 2022. Environmental Mapping and Analysis Program (EnMAP). www.enmap.org.

EROS, 2022. EROS Cal/Val Center of Excellence. calval.cr.usgs.gov/apps/test_sites_catalog.

Fontenla, J.M., Harder, J., Livingston, W., Snow, M., Woods, T., 2011. High-resolution solar spectral irradiance from extreme ultraviolet to far infrared. J. Geophys. Res.: Atmos. 116, http://dx.doi.org/10.1029/2011JD016032.

Gnat, M., 2022. Ground station network. In: Sellmaier, F., Schmidhuber, M., Uhlig, T. (Eds.), Spacecraft Operations Book, Springer Aerospace Technology. SAT, Springer, pp. 181–196. http://dx.doi.org/10.1007/978-3-030-88593-9.

Green, R.O., Eastwood, M.L., Sarture, C.M., Chrien, T.G., Aronsson, M., Chippendale, B.J., Faust, J.A., Pavri, B.E., Chovit, C.J., Solis, M., et al., 1998. Imaging spectroscopy and the Airborne Visible/InfraRed Imaging Spectrometer (AVIRIS). Remote Sens. Environ. 65 (3), 227–248. http://dx.doi.org/10.1016/S0034-4257(98)00064-9.

Guanter, L., Kaufmann, H., Segl, K., Foerster, S., Rogass, C., Chabrillat, S., Kuester, T., Hollstein, A., Rossner, G., Chlebek, C., Straif, C., Fischer, S., Schrader, S., Storch, T., Heiden, U., Mueller, A., Bachmann, M., Mühle, H., Müller, R., Habermeyer, M., Ohndorf, A., Hill, J., Buddenbaum, H., Hostert, P., Van der Linden, S., Leitão, P.J., Rabe, A., Doerffer, R., Krasemann, H., Xi, H., Mauser, W., Hank, T., Locherer, M., Rast, M., Staenz, K., Sang, B., 2015. The EnMAP spaceborne imaging spectroscopy mission for Earth observation. Remote Sens. 7 (7), 8830–8857. http://dx.doi.org/10.3390/rs70708830.

Guanter, L., Segl, K., Sang, B., Alonso, L., Kaufmann, H., Moreno, J., 2009. Scene-based spectral calibration assessment of high spectral resolution imaging spectrometers. Opt. Express 17 (14), http://dx.doi.org/10.1364/OE.17.011594.

Habermeyer, M., Pinnel, N., Storch, T., Honold, H.-P., Tucker, P., Guanter, L., Segl, K., Fischer, S., 2019. The EnMAP mission: From observation request to data delivery. In: Proceedings of the 2019 IEEE International Geoscience and Remote Sensing Symposium. IGARSS, pp. 4507–4510. http://dx.doi.org/10.1109/IGARSS.2019.8897821.

Heller Pearlshtien, D., Ben-Dor, E., 2022. CalVal evaluation of DESIS products in Amiaz Plain and Makhtesh Ramon test sites, Southern Israel. Int. Arch. Photogramm. Remote Sens. Spat. Inf. Sci. XLVI-1/W1-2021, 13–21. http://dx.doi.org/10.5194/isprs-archives-XLVI-1-W1-2021-13-2022.

HYPERNETS, 2022. HYPERNETS. hypernets.eu.

Kahle, R., Aida, S., Trullàs, M., Lück, S., Schlepp, B., Schoutetens, F., 2022. Flight dynamics experience on target orbit acquisition and maintenance operations for Germany's hyperspectral satellite mission EnMAP. In: Proceedings of 28th International Symposium on Space Flight Dynamics. ISSFD, pp. 1–12.

Kahle, R., Spiridonova, S., Kirschner, M., 2019. Improved reference orbits for the repeat-ground-track missions EnMAP and Tandem-L. Trans. Jpn. Soc. Aeronaut. Space Sci. Aerosp. Technol. Jpn. 17 (3), 308–314. http://dx.doi.org/10.2322/tastj.17.308.

Kaufmann, H., Sang, B., Storch, T., Segl, K., Förster, S., Guanter, L., Erhard, M., Heider, B., Hofer, S., Honold, H.-P., Penné, B., Bachmann, M., Habermeyer, M., Müller, A., Müller, R., Rast, M., Staenz, K., Straif, C., Chlebek, C., 2016. Environmental Mapping and Analysis Program—A German hyperspectral mission. In: Qian, S.-E. (Ed.), Optical Payloads for Space Missions. John Wiley & Sons, pp. 161–182. http://dx.doi.org/10.1002/9781118945179.

Keremedjiev, M., Haag, J., Shivers, S., Guido, J., Roth, K., teja Nallapu, R., Dockstader, S., McGill, L., Giuliano, P., Duren, R., Asner, G.P., 2022. Carbon mapper phase 1: two upcoming VNIR-SWIR hyperspectral imaging satellites. In: Proceedings of SPIE, Algorithms, Technologies, and Applications for Multispectral and Hyperspectral Imaging XXVIII, Vol. 12094. 1209409. http://dx.doi.org/10.1117/12.2632547.

Kiselev, V., Bulgarelli, B., Heege, T., 2015. Sensor independent adjacency correction algorithm for coastal and inland water systems. Remote Sens. Environ. 157, 85–95. http://dx.doi.org/10.1016/j.rse.2014.07.025.

Köhler, C.H., 2016. Airborne imaging spectrometer HySpex. J. Large-Scale Res. Facil. 2, http://dx.doi.org/10.17815/jlsrf-2-151.

Müller, R., Lehner, M., Reinartz, P., Schroeder, M., 2005. Evaluation of spaceborne and airborne line scanner images using a generic ortho image processor. In: Proceedings of High Resolution Earth Imaging for Geospatial Information 2005, IAPRS, Volume XXXVI. pp. 1–6.

Ong, C., Caccetta, M., Lau, I., Ong, L., Middleton, E., 2017. Compositional characterisation of the Pinnacles vicarious calibration site. In: Proceedings of 2017 IEEE International Geoscience and Remote Sensing Symposium. IGARSS, pp. 3059–3062. http://dx.doi.org/10.1109/IGARSS.2017.8127644.

Pearlman, J.S., Barry, P.S., Segal, C.C., Shepanski, J., Beiso, D., Carman, S.L., 2003. Hyperion, a space-based imaging spectrometer. IEEE Trans. Geosci. Remote Sens. 41 (6), 1160–1173. http://dx.doi.org/10.1109/TGRS.2003.815018.

Platnick, S., Meyer, K.G., King, M.D., Wind, G., Amarasinghe, N., Marchant, B., Arnold, G.T., Zhang, Z., Hubanks, P.A., Holz, R.E., et al., 2016. The MODIS cloud optical and microphysical products: Collection 6 updates and examples from Terra and Aqua. IEEE Trans. Geosci. Remote Sens. 55 (1), 502–525. http://dx.doi.org/10.1109/TGRS.2016.2610522.

RadCalNet, 2022. Radiometric Calibration Network Portal. www.radcalnet.org.

de los Reyes, R., Langheinrich, M., Schwind, P., Richter, R., Pflug, B., Bachmann, M., Müller, R., Carmona, E., Zekoll, V., Reinartz, P., 2020. PACO: Python-based atmospheric correction. Sensors 20 (5), http://dx.doi.org/10.3390/s20051428.

Sang, B., Schubert, J., Kaiser, S., Mogulsky, V., Neumann, C., Förster, K.-P., Hofer, S., Stuffler, T., Kaufmann, H., Müller, A., Eversberg, T., Chlebek, C., 2008. The EnMAP hyperspectral imaging spectrometer: instrument concept, calibration, and technologies. In: Proceedings of SPIE, Imaging Spectrometry XIII, Vol. 7086. pp. 1–15. http://dx.doi.org/10.1117/12.794870.

Scheffler, D., Hollstein, A., Diedrich, H., Segl, K., Hostert, P., 2017. AROSICS: An Automated and Robust Open-Source Image Co-Registration Software for multi-sensor satellite data. Remote Sens. 9 (7), http://dx.doi.org/10.3390/rs9070676.

Schneider, M., Müller, R., Krawczyk, H., Bachmann, M., Storch, T., Mogulsky, V., Hofer, S., 2012. The future spaceborne hyperspectral imager EnMAP: Its in-flight radiometric and geometric calibration concept. In: Proceedings of ISPRS 2012, ISPRS International Archives of the Photogrammetry, Remote Sensing and Spatial Information Sciences, Volume XXXIX-B1. pp. 267–272. http://dx.doi.org/10.5194/isprsarchives-XXXIX-B1-267-2012.

Schroeder, T., Schaale, M., Lovell, J., Blondeau-Patissier, D., 2022. An ensemble neural network atmospheric correction for Sentinel-3 OLCI over coastal waters providing inherent model uncertainty estimation and sensor noise propagation. Remote Sens. Environ. 270, http://dx.doi.org/10.1016/j.rse.2021.112848.

Schwind, P., Müller, R., Palubinskas, G., Storch, T., 2012. An in-depth simulation of EnMAP acquisition geometry. ISPRS J. Photogramm. Remote Sens. 70, 99–106. http://dx.doi.org/10.1016/j.isprsjprs.2012.03.012.

Soja-Woźniak, M., Baird, M., Schroeder, T., Qin, Y., Clementson, L., Baker, B., Boadle, D., Brando, V., Steven, A.D., 2019. Particulate backscattering ratio as an indicator of changing particle composition in coastal waters: Observations from Great Barrier Reef waters. J. Geophys. Res.: Oceans 124 (8), 5485–5502. http://dx.doi.org/10.1029/2019JC014998.

Storch, T., Habermeyer, M., Eberle, S., Mühle, H., Müller, R., 2013. Towards a critical design of an operational ground segment for an Earth observation mission. J. Appl. Remote Sens. 7 (1), 1–12. http://dx.doi.org/10.1117/1.JRS.7.073581.

Storch, T., Honold, H.-P., Alonso, K., Pato, M., Mücke, M., Basili, P., Chabrillat, S., Fischer, S., 2020. Status of the imaging spectroscopy mission EnMAP with radiometric calibration and correction. In: Proceedings of ISPRS 2020, ISPRS Annals of the Photogrammetry, Remote Sensing and Spatial Information Sciences, Volume V-1. pp. 41–47. http://dx.doi.org/10.5194/isprs-annals-V-1-2020-41-2020.

Storch, T., Honold, H.-P., Guanter, L., Schwind, P., Mücke, M., Segl, K., Fischer, S., 2018a. The imaging spectroscopy mission EnMAP—Its status and expected products. In: Proceedings of WHISPERS 2018.

Storch, T., Honold, H.-P., Krawczyk, H., Wachter, R., de los Reyes, R., Langheinrich, M., Mücke, M., Fischer, S., 2018b. Spectral characterization and smile correction for the imaging spectroscopy mission EnMAP. In: Proceedings of 2018 IEEE International Geoscience and Remote Sensing Symposium. IGARSS, pp. 3304–3306. http://dx.doi.org/10.1109/IGARSS.2018.8517573.

Thompson, D.R., Basilio, R., Brosnan, I., Cawse-Nicholson, K., Chadwick, K.D., Guild, L., Gierach, M., Green, R.O., Hook, S., Horner, S.D., Hulley, G., Kokaly, R., Miller, C.E., Miner, K.R., Lee, C., Limonadi, D., Luvall, J., Pavlick, R., Phillips, B., Poulter, B., Raiho, A., Reath, K., Uz, S.S., Sen, A., Serbin, S., Schimel, D., Townsend, P., Turner, W., Turpie, K., The SBG Team, 2022. Ongoing progress toward NASA's Surface Biology and Geology mission. In: Proceedings of 2022 IEEE International Geoscience and Remote Sensing Symposium. IGARSS, pp. 5007–5010. http://dx.doi.org/10.1109/IGARSS46834.2022.9884123.

Thuillier, G., Hersé, M., Foujols, T., Peetermans, W., Gillotay, D., Simon, P., Mandel, H., et al., 2003. The solar spectral irradiance from 200 to 2400 nm as measured by the SOLSPEC spectrometer from the ATLAS and EURECA missions. Sol. Phys. 214 (1), 1–22. http://dx.doi.org/10.1023/A:1024048429145.

Urai, M., Tsuchida, S., Yamamoto, S., Tachikawa, T., Iwasaki, A., M, Ishii, J., 2021. Initial onboard calibration results of the HISUI hyperspectral sensor. In: Proceedings of 2021 IEEE International Geoscience and Remote Sensing Symposium. IGARSS, pp. 1608–1610. http://dx.doi.org/10.1109/IGARSS47720.2021.9554224.

Wan, Z., 2014. New refinements and validation of the collection 6 MODIS land-surface temperature/emissivity product. Remote Sens. Environ. 140, 36–45. http://dx.doi.org/10.1016/j.rse.2013.08.027.

Werdell, P., Behrenfeld, M., Bontempi, P., Boss, E., Cairns, B., Davis, G., Franz, B., Gliese, U., Gorman, E., Hasekamp, O., Knobelspiesse, K., Mannino, A., Martins, V., Mcclain, C., Meister, G., Remer, L., 2019. The Plankton, Aerosol, Cloud, ocean Ecosystem (PACE) mission: Status, science, advances. Bull. Am. Meteorol. Soc. 100, http://dx.doi.org/10.1175/BAMS-D-18-0056.1.

Zibordi, G., Mélin, F., Berthon, J.-F., Holben, B., Slutsker, I., Giles, D., D'Alimonte, D., Vandemark, D., Feng, H., Schuster, G., et al., 2009. AERONET-OC: a network for the validation of ocean color primary products. J. Atmos. Ocean. Technol. 26 (8), 1634–1651. http://dx.doi.org/10.1175/2009JTECHO654.1.